Waveguiding driven by the Pancharatnam-Berry phase

Chandroth P. Jisha [1,*] Stree Vithya Arumugam,[1] Lorenzo Marrucci,[2] Stefan Nolte [1,3] and Alessandro Alberucci [1,†]

[1]*Friedrich Schiller University Jena, Institute of Applied Physics, Abbe Center of Photonics, Albert-Einstein-Str. 15, 07745 Jena, Germany*

[2]*Dipartimento di Fisica "Ettore Pancini," Università di Napoli Federico II, Complesso Universitario di Monte Sant'Angelo, Via Cintia, 80126 Napoli, Italy*

[3]*Fraunhofer Institute for Applied Optics and Precision Engineering IOF, Albert-Einstein-Str. 7, 07745 Jena, Germany*

(Received 7 September 2022; revised 22 December 2022; accepted 9 January 2023; published 26 January 2023)

We theoretically and numerically investigate the properties of waveguides based on the Pancharatnam-Berry phase, obtained by a longitudinally periodic rotation of the optic axis in a transversely twisted birefringent medium. In this paper we study the case where the period of the longitudinal modulation is chosen so that a net accumulation of geometric phase in propagation occurs. First, the interplay between different contributions to the optical potential is addressed. Second, a continuous evolution of the polarization structure of the quasimodes is observed in the numerical simulations. We explain it by a combination of plane-wave-based models and gauge transformations. We discover that, beyond the longitudinal oscillations, the polarization of the quasimode also varies through its cross section. The analogies with respect to charged particles moving in a magnetic field are outlined.

DOI: 10.1103/PhysRevA.107.013523

I. PANCHARATNAM-BERRY PHASE IN TWISTED ANISOTROPIC MATERIALS

The propagation of plane waves in homogeneous anisotropic media is well understood: their refractive index depends on the direction of the electric field, with in general a nonparallel condition between the electric field $\boldsymbol{E}$ and the displacement vector $\boldsymbol{D}$ [1]. Mathematically, anisotropic materials are defined by a dielectric tensor $\boldsymbol{\epsilon}_D = \mathrm{diag}(\epsilon_{x'x'}, \epsilon_{y'y'}, \epsilon_{z'z'})$, where x', y', z' identify the principal dielectric axes. In uniaxial materials, two eigenvalues, namely, $\epsilon_{x'x'}$ and $\epsilon_{z'z'}$, are identical and named $\epsilon_\perp$, whereas $\epsilon_{y'y'} = \epsilon_\parallel$ is the dielectric constant along the optic axis $\hat{n} = \hat{y}'$, see Fig. 1(a). When the wave vector $\boldsymbol{k}$ is normal to the optic axis, the two independent eigenmodes are the extraordinary and ordinary waves, perceiving respectively the refractive indexes $n_\parallel = \sqrt{\epsilon_\parallel}$ and $n_\perp = \sqrt{\epsilon_\perp}$. This is the configuration used in wave plates, which control the light polarization via the phase retardation $\Delta\phi = k_0 \Delta n L$, where $\Delta n = n_\parallel - n_\perp$ is the birefringence, k_0 is the vacuum wave number, and L is the length of the anisotropic material along the propagation direction z. From a mathematical point of view, the propagation of optical plane waves in anisotropic materials can be described using the Jones formalism, where a two-component vector fully determines the electromagnetic field [2].

A surprising new effect arises when the Jones calculus is applied to a twisted anisotropic material, i.e., a material whose optic axis varies across the transverse plane xy orthogonal to the wave vector $\boldsymbol{k}$. If we name θ the angle between the optic axis and the axis y [see Fig. 1(a)], when $\Delta\phi = \pi$ (half-wave plate, HWP) a circular polarized beam accumulates a transverse phase modulation given by $\pm 2\theta(x, y)$, the sign depending on the handedness of the impinging photons [3,4] [see Fig. 1(b)]. This phase term is a manifestation of geometric phase, which is added to the dynamic phase (the optical path in optics) occurring when the Hamiltonian of a system is subject to a change in propagation [5]. First introduced in a quantum-mechanical framework and in the presence of a periodic evolution by Sir Michael Berry in 1984 [6], a specific type of geometric phase was actually discovered by Pancharatnam 30 years earlier while studying polarized waves [7]. In the presence of a varying polarization along the propagation direction z, Pancharatnam found that an optical beam acquires a phase proportional to the corresponding area subtended by the polarization state trajectory on the Poincaré sphere. When the polarization trace of a circularly polarized beam propagating in a wave plate is drawn on the Poincaré sphere, it is evident that the phase term $\pm 2\theta$ is a manifestation of the mechanism described by Pancharatnam (for a more detailed discussion see Sec. II A). Berry showed that, for a helicity α, the application of the Pancharatnam's idea to this case provides [3]

$$\Delta\varphi_{\mathrm{geo}}(\zeta) = \arg\left[\cos^2\left(\frac{\zeta}{2}\right) + \sin^2\left(\frac{\zeta}{2}\right) e^{2i\alpha(\theta_2-\theta_1)}\right], \quad (1)$$

where $\Delta\varphi_{\mathrm{geo}}$ is the phase delay observed when two optical beams propagate in two anisotropic material encompassing a relative rotation $\theta_2 - \theta_1$, computed for the z-dependent phase retardation $\zeta = k_0 \Delta n z$. For small relative rotations $\theta_2 - \theta_1$, the geometric delay $\Delta\varphi_{\mathrm{geo}}$ follows a sinusoidal trend versus the propagation distance, see, e.g., Fig. 1(b). This phase is

*jisha.chandroth.pannian@uni-jena.de
†alessandro.alberucci@uni-jena.de

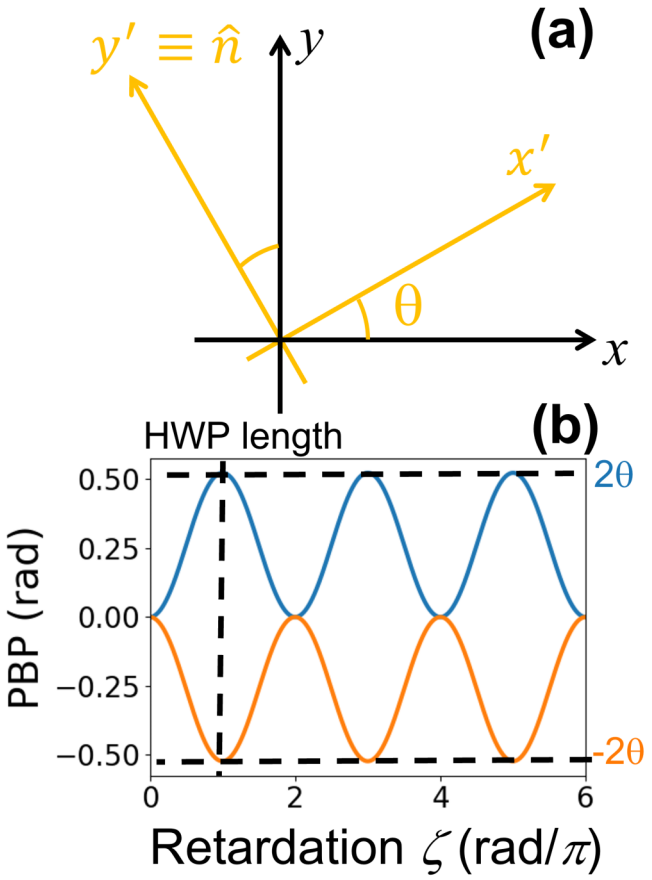

FIG. 1. Optical propagation in a rotated anisotropic material. (a) Definition of the local reference system $x'y'z'$ rotated of an angle θ with respect to the laboratory framework xyz. In $x'y'z'$ the dielectric tensor is always diagonal. (b) PBP delay between light propagation in xyz and $x'y'z'$ versus the retardation ζ in the case of circularly polarized plane waves. The rotation angle θ is 15°.

today called the Pancharatnam-Berry phase (PBP) in honor of its two fathers [8].

Probably due to technological constraints in manufacturing twisted anisotropic materials, the idea of wave front manipulation through the PBP has not been pursued until early in 2000, the year in which the first experimental demonstration was accomplished using subwavelength metallic gratings with a point-dependent orientation [9]. The idea was applied some years later in liquid crystals, where the local optic axis can be controlled by a proper shaping of the boundary conditions [10–12]. The field literally exploded when wave front shaping was demonstrated in metasurfaces, ultrathin metamaterials featuring subwavelength structures. To observe PBP modulation, the basic elements of metasurface must lack rotational symmetry, thus mimicking the response of an anisotropic material [13–16]. Currently, PBP is a central topic in modern optics, setting a new frontier for the control of light propagation [8].

As stated above, the phase modulation proportional to the local twist angle appears when the material is an infinitely thin HWP; that is, the propagation distance is negligible with respect to the Rayleigh distance of the beam. The interplay between diffraction and PBP has been investigated both in longitudinally invariant and periodically modulated twisted geometries, where the PBP action is modeled by effective potential(s) dependent on the local rotation angle θ [17–20]. In both cases, it has been demonstrated how the effective potential acting on the photons can be tailored to realize optical waveguides even in the absence of a gradient in the refractive index [19,20], with potential applications in topological photonics [21]. In this paper we use the more compact name Berry waveguide. Finally, the existence of the potential has been demonstrated experimentally in the nonlinear regime in liquid crystals [22].

Here we investigate theoretically and numerically the optical propagation in a twisted material, periodically modulated with a period $\Lambda = \lambda/\Delta n$ to allow the accumulation of PBP in propagation, with an approach that recalls quasiphase matching in nonlinear optics. We discuss how the polarization structure of the localized quasimode evolves as the twisting of the material is increased. We show how higher-order effects, related with the nonadiabatic changes in the material parameters and mainly modeled via local gauge transformations, deeply impact light propagation. We emphasize how the point-dependent twisting of the material is responsible for a very strong spin-orbit interaction, the latter being tunable with the maximum rotation angle applied to the medium.

II. OPTICAL PROPAGATION IN A PERIODIC ANISOTROPIC STRUCTURE

Neglecting the longitudinal component along the propagation distance z, the electric field can be depicted as a two-component vector $\boldsymbol{\psi} = (E_x; E_y)$. The approximate field $\boldsymbol{\psi}$ then obeys the vectorial Helmholtz equation $\nabla^2\boldsymbol{\psi} + k_0^2\boldsymbol{\epsilon}\cdot\boldsymbol{\psi} = 0$, where $\boldsymbol{\epsilon}$ is determined by the local twist angle $\theta(x, y, z)$. Given that the longitudinal component is neglected, hereafter we restrict the dielectric tensor $\boldsymbol{\epsilon}$ to the transverse xy components. Specifically, it is $\boldsymbol{\epsilon} = \boldsymbol{R}^{-1}(\theta)\cdot\boldsymbol{\epsilon}_D\cdot\boldsymbol{R}(\theta)$, where $\boldsymbol{R}(\theta) = (\cos\theta, \sin\theta; -\sin\theta, \cos\theta)$. The dielectric permittivity tensor can also be written as $\epsilon_{ij} = \delta_{ij}\epsilon_\perp + \epsilon_a n_i n_j$ $(i, j = x, y, z)$ [23], where $\epsilon_a = \epsilon_\parallel - \epsilon_\perp$ is the optical anisotropy. Given that we allow only for rotations of the optic axis in the plane xy, the relative dielectric permittivity tensor is

$$\boldsymbol{\epsilon} = \epsilon_\perp \boldsymbol{I} + \epsilon_a \begin{pmatrix} \sin^2\theta & -\cos\theta\sin\theta \\ -\cos\theta\sin\theta & \cos^2\theta \end{pmatrix}. \tag{2}$$

Incidentally, in terms of the Pauli matrices $\boldsymbol{\sigma}_i$ $(i = 1, 2, 3)$, it is $\boldsymbol{R}(\theta) = e^{i\boldsymbol{\sigma}_2\theta(x,y,z)}$, where we recall that $\sigma_1 = (0, 1; 1, 0)$, $\sigma_2 = (0, -i; i, 0)$, and $\sigma_3 = (1, 0; 0, -1)$. The two-component electric field obeys

$$\nabla^2\boldsymbol{\psi} + k_0^2\left\{\overline{\epsilon}\boldsymbol{I} - \frac{\epsilon_a}{2}[\boldsymbol{\sigma}_1\sin(2\theta) + \boldsymbol{\sigma}_3\cos(2\theta)]\right\}\cdot\boldsymbol{\psi} = 0, \tag{3}$$

where $\overline{\epsilon} = (\epsilon_\perp + \epsilon_\parallel)/2$. Terms proportional to the optical anisotropy ϵ_a can be rearranged in the form of a magnetic interaction

$$H_{\rm per} = -\frac{\epsilon_a}{2}[\boldsymbol{\sigma}_1\sin(2\theta) + \boldsymbol{\sigma}_3\cos(2\theta)] = \frac{1}{2}\boldsymbol{\sigma}\cdot\boldsymbol{B}_{\rm eff}, \tag{4}$$

where we introduced the Pauli vector $\boldsymbol{\sigma} = \boldsymbol{\sigma}_1\hat{e}_1 + \boldsymbol{\sigma}_2\hat{e}_2 + \boldsymbol{\sigma}_3\hat{e}_3$ and where $\boldsymbol{B}_{\rm eff} = -\epsilon_a[\sin(2\theta)\hat{e}_1 + \cos(2\theta)\hat{e}_3]$

represents an effective magnetic field [24–26], here defined within a three-dimensional vector space spanned by unit vectors $\hat{e}_i$ $(i = 1, 2, 3)$. Following our definition, $\boldsymbol{B}_{\text{eff}}$ is antiparallel to $\hat{e}_3$ for $\theta = 0$. Invariance to global rotation is automatically satisfied by the scalar product in Eq. (4). Finally, given that rotations of 180° do not vary the optical properties of the anisotropic slab, the angle formed by $\boldsymbol{B}_{\text{eff}}$ in the e_1e_3 plane is double the physical angle made by the optic axis in the transverse plane xy.

Once rewritten in the paraxial limit, Eq. (3) closely recalls the Pauli equation for a massive particle subject to a homogeneous scalar potential (term proportional to $\overline{\epsilon}$) and to a fictitious magnetic field having a constant amplitude but a changing direction within the plane the plane e_1e_3. In optical terms, this shows that there are no refractive index gradients in this configuration. The effective magnetic field also explains the fundamental role played by geometric phase in driving the optical propagation [8,27].

For the sake of simplicity, hereafter we focus on the $(1 + 1)$D case setting $\partial_y = 0$. To correctly apply the paraxial conditions, we rewrite the field $\boldsymbol{\psi}$ in an inhomogeneously rotated system $\boldsymbol{\psi}' = \boldsymbol{R}[\theta(x, z)] \cdot \boldsymbol{\psi}$, i.e., we apply a local gauge transformation. A similar approach is used when describing the Majorana spin flip occurring, for example, in magnetic traps [28]. Given the dielectric tensor is now diagonal everywhere, the light wave fulfills the following vectorial equation [19]:

$$\frac{\partial^2\boldsymbol{\psi}'}{\partial z^2} - i\boldsymbol{\sigma_2}\cdot\left(2\frac{\partial\theta}{\partial z}\frac{\partial\boldsymbol{\psi}'}{\partial z} + \frac{\partial^2\theta}{\partial z^2}\boldsymbol{\psi}'\right) + k_0^2\boldsymbol{\epsilon}_D\cdot\boldsymbol{\psi}' - \left(\frac{\partial\theta}{\partial z}\right)^2\boldsymbol{\psi}' = -\frac{\partial^2\boldsymbol{\psi}'}{\partial x^2} + \left(\frac{\partial\theta}{\partial x}\right)^2\boldsymbol{\psi}' + i\frac{\partial^2\theta}{\partial x^2}\boldsymbol{\sigma_2}\cdot\boldsymbol{\psi}' + 2i\frac{\partial\theta}{\partial x}\boldsymbol{\sigma_2}\cdot\frac{\partial\boldsymbol{\psi}'}{\partial x}. \tag{5}$$

The left-hand side (LHS) of Eq. (5) models the propagation of plane waves in a longitudinally rotated twisted material, with no gradients along the transverse direction x. Let us now define the 2×2 matrix $\boldsymbol{N} = (n_\perp, 0; 0, n_\parallel)$. The paraxial approximation (i.e., setting $\partial_z^2\boldsymbol{\psi}' = 0$) is correctly applied to Eq. (5) if the transformation $\boldsymbol{\psi}' = e^{ik_0\boldsymbol{N}z}\cdot\boldsymbol{u}$ is carried out, where $\boldsymbol{u}$ is the slowly varying vectorial envelope. Remarkably, the rotating field transformation factors out the different phase velocities of the ordinary and extraordinary components: for example, a field $\boldsymbol{u}$ featuring a circular polarization conserves its polarization in propagation.

We now specialize our treatment to periodic modulations of the twisting angle along the propagation direction by setting $\theta(x, z) = H(z)\Gamma(x)$; that is, the spatial dependence of the twisting angle θ can be separated. The function $\Gamma(x)$ provides the transverse shape of the rotation angle, whereas the periodic function $H(z) = H(z + \Lambda)$ determines the modulation of the rotation along the propagation direction z. We further assume $\Lambda = \lambda/\Delta n$, where $\lambda/\Delta n$ is the birefringence period providing the natural oscillation of the optical polarization in the material (i.e., the full wave plate length). This matching between the natural oscillation and the external modulation allows a net accumulation of PBP in propagation [19].

As described by Eq. (5), to first approximation optical propagation in twisted anisotropic materials has strong similarities with the same process in inhomogeneous isotropic materials: (i) a diffraction operator tending to broaden the beam along the transverse direction; (ii) a wave front modulation proportional to the transverse gradient in the optical properties of the material. In our case the gradient is imposed on the twisting angle and provides a point-dependent phase modulation associated with a change in the polarization with z. Actually, an intuitive model can be formulated by investigating the propagation of plane waves (i.e., in the absence of diffraction) in materials that are treated as homogeneous along the transverse direction x but change periodically along the propagation direction z. Physically speaking, this approach is exact for very slow rotations of the optical axis along the transverse direction x. In the limit of small birefringence Δn, this case can be solved by applying the Jones' formalism to a stack of infinitely thin layers (see Appendix B). With the assumptions made, the optical propagation depends only on the phase retardation $\zeta = k_0\Delta n z$. The interplay with diffraction can then be accounted for in a second stage.

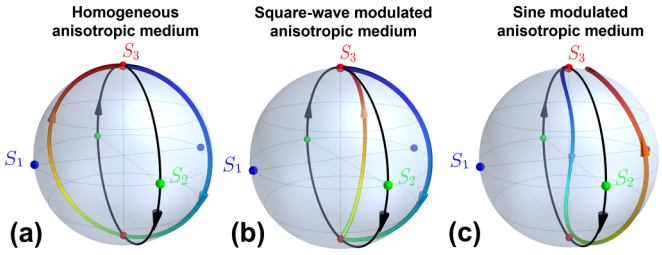

FIG. 2. Polarization evolution of initially CP plane waves mapped on the Poincaré sphere for three different longitudinal modulation of the rotation angle. The profile of θ is (a) uniform along z, (b) a square wave, and (c) a sinusoidal modulation. The maximum rotation angle is $\pi/8$ in all the three cases. The black curve in each panel is the case for a uniform and vanishing angle θ.

A. Plane-wave solution in the presence of a longitudinal modulation of the twisting angle

Let us start from a brief summary of the circularly polarized (CP) plane-wave propagation in an anisotropic material where the longitudinal modulation follows a square-wave function of duty cycle 50%, and its behavior in comparison with the longitudinally homogeneous case. Figure 2(a) shows that the polarization on the Poincaré sphere in a homogeneous anisotropic medium traces meridians, which one being dictated by the rotation angle θ. By computing the solid area of the corresponding closed path, for a distance $z = \Lambda/2$ (HWP length) a phase retardation $2(\theta_2 - \theta_1)$—corresponding to the solid angle subtended by the path on the Poincaré sphere [7]—between differently rotated axes is accumulated, see also Eq. (1). In the next half period (i.e., up to $z = \Lambda$), the accumulated phase delay vanishes because the same amount of phase delay but inverted in sign (in the Pancharatnam approach the clockwise or counterclockwise nature of the oriented closed path has to be accounted for [7,8]) is summed up. Thus, no net accumulation in propagation is occurring, in agreement with Eq. (1).

From the geometrical interpretation, a simple solution to accumulate PBP in propagation is to modify the motion of the polarization in the Poincaré sphere in the second half period,

$\Lambda/2 < z < \Lambda$. This can be accomplished by changing the direction of the optic axis θ in the second half period. The easiest case is the symmetrical one: the optic axis is flipped with respect to the y axis by setting $\theta \to -\theta$ at the end of the first half period ($z = \Lambda/2$, HWP distance). As shown in Fig. 2(b), the paths along the two half periods are geometrically equivalent, yielding a total phase accumulation of $4(\theta_2 - \theta_1)$. In the perspective of Eq. (1), the sign of α needs to be changed to account for the mirror flipping operated on the optic axis. Given we used a generic relative rotation $\theta_2 - \theta_1$, our considerations hold valid when the position $\theta_2 - \theta_1 \to H(z)\Gamma(x)$ is made, where $H(z)$ is a square wave of duty cycle 50%. Thus, after propagating across a length Λ the field returns to its initial polarization state, but has acquired a phase delay of geometric origin equal to $4\Gamma(x)$ [8]. This cycle can then be repeated, leading to a progressive accumulation of a transverse phase gradient of geometric origin. The full behavior of the Stokes parameter is plotted in Fig. 10(a) in Appendix A.

We now turn our attention to the case of a sinusoidal longitudinal modulation of the optical axis, thus avoiding abrupt discontinuities along the optical path. The polarization path for one birefringence length is plotted in Fig. 2(c). PBP is still accumulated, but with a value now given by $\pi\Gamma$ for small angles (see next section for details) [19]. As a matter of fact, a smaller area than the square wave modulation is enclosed by the path. The most important difference is that the final point does not correspond anymore to the initial one. As shown in the next section, the eigenvectors in this case comprise a nonvanishing S_1 component; that is, the path does not cross the two poles. Consequently, the plane-wave propagation already proves that the exact quasimodes are not circularly polarized, at least in a PBP waveguide when a nonvanishing and finite longitudinal gradient in θ is present.

B. Quasimodes in the transversely homogeneous case

Due to the periodic nature of the system, eigenwaves of the system can be found considering one single oscillation period, $z \in [z_0, z_0 + \Lambda]$. Hereafter we consider only sinusoidal waveforms for $H(z)$. We also fix $\Gamma(x) = \Gamma_0 f(x)$, where the peak of $f(x)$ is equal to unity; accordingly, the scalar parameter Γ_0 is the maximum rotation applied to the anisotropic material. The numerically computed eigenvectors and eigenvalues in the case $\theta(z) = \Gamma_0 \sin(2\pi z/\Lambda)$ are plotted as a function of Γ_0 in Fig. 3 (see Appendix B for the employed numerical method). For a vanishing Γ_0, the polarization states move along the meridian of the Poincaré sphere containing both the poles (CPs) and the diagonal or antidiagonal linear polarization (defined with respect to the reference system xy). Stated otherwise, there is a sinusoidal oscillation of the Stokes parameters S_2 and S_3, while S_1 is null in every point of the path (see, e.g., Fig. 10 in Appendix A). As Γ_0 assumes small but finite values, the trajectory moves away from the meridian and acquires a small component along S_1, see Fig. 3(a) [29]. Up to $\Gamma_0 \approx 45°$, the S_1 value increase of the eigenstate is linear with Γ_0. The growth of S_1 then gets steeper, with an inflection point around $\Gamma_0 \approx 110°$ and eventually reaching a local maximum around $\Gamma_0 \approx 117°$. After the local maximum,

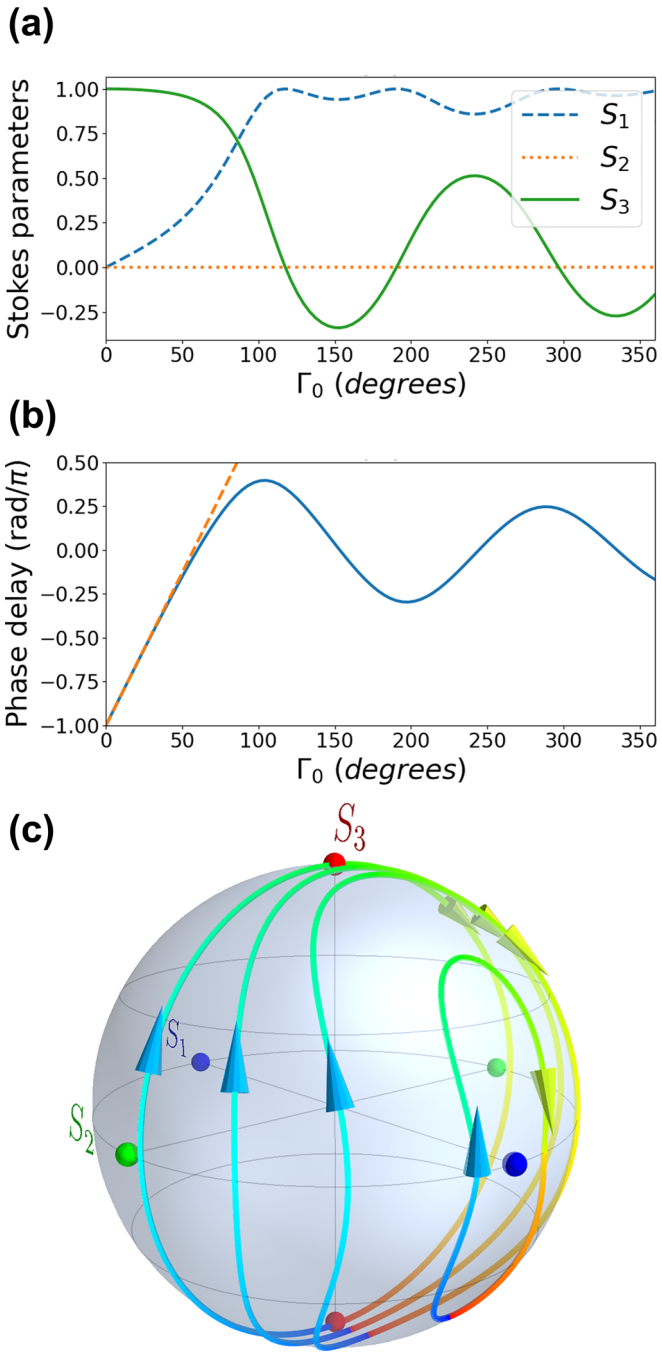

FIG. 3. Properties of quasimodes in a sinusoidally rotated anisotropic material infinitely extended along the transverse direction. (a) Stokes parameters of the eigenmode (corresponding to the polarization assumed at the start of each longitudinal period) and (b) the corresponding geometric phase delay $\Delta\varphi_{\text{geo}}$ gained across a single rotation period versus the maximum rotation angle Γ_0. In panel (c) the evolution of the eigenmodes over the Poincaré sphere is shown for $\Gamma_0 = 4°, 24°, 44°$, and $86°$, from the longest to the smallest circuit, respectively. The dashed line in panel (b) corresponds to the geometric phase computed under the small rotation approximation, providing $\Delta\varphi_{\text{geo}} = \pi\Gamma_0$. Due to the symmetry of the system, another set of eigenmodes with opposite Stokes parameters and opposite phase delay exists.

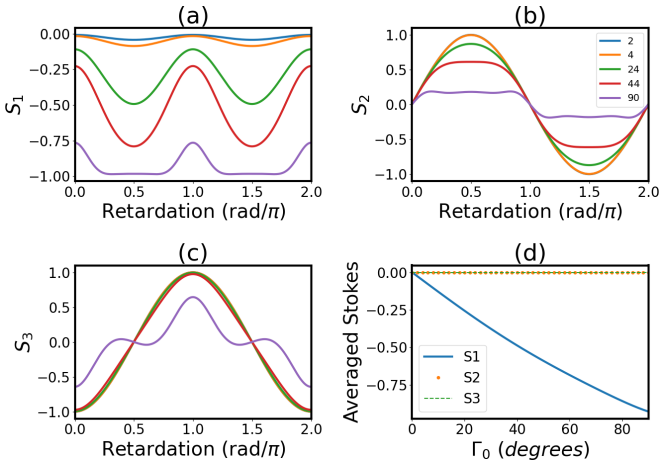

FIG. 4. Longitudinal evolution of the quasimodes shown in Fig. 3. Behavior versus z of the Stokes parameters (a) S_1, (b) S_2, and (c) S_3 versus the phase retardation $\zeta = k_0 \Delta n z$. The corresponding maximum rotation angles Γ_0 are reported in the legend in panel (b). (d) Average of the Stokes parameters over one birefringence length versus the angle Γ_0.

S_1 oscillates close to the maximum possible value $S_1 = 1$ in a quasiperiodic fashion. The oscillation period varies between 70° and 90°. Remarkably, S_2 is always vanishing, no matter how large the rotation angle is. The accumulated phase delay plotted in Fig. 3(b) is linearly increasing versus Γ_0 for small S_1, then undergoing a downwards bending around $S_1 = 0.25$. For large enough S_1, the accumulated PBP varies in a nonmonotonic fashion, following the changes in the polarization, as first pointed out by Pancharatnam. An overview of the polarization paths on the Poincaré sphere for four values of Γ_0 is shown in Fig. 3(c).

From the theoretical side, in the limit of small anisotropy $\gamma = \Delta n/\bar{n} \ll 1$, plane wave obeys the following vectorial equation (details of the computation can be found in Appendix A):

$$i\frac{\partial \boldsymbol{u}}{\partial \zeta} = -\frac{\partial \theta}{\partial \zeta}[\sin(\zeta)\boldsymbol{\sigma}_1 + \cos(\zeta)\boldsymbol{\sigma}_2] \cdot \boldsymbol{u}, \tag{6}$$

where ζ is the phase retardation introduced earlier. In the resonant case $\theta(\zeta) = \Gamma_0 \sin(\zeta)$, and Eq. (6) yields

$$i\frac{\partial \boldsymbol{u}}{\partial \zeta} = -\frac{\Gamma_0}{2}[\sin 2\zeta\ \boldsymbol{\sigma}_1 + (1 + \cos 2\zeta)\boldsymbol{\sigma}_2] \cdot \boldsymbol{u}. \tag{7}$$

We are interested in the averaged behavior of the field versus ζ. We thus neglect the oscillating terms explicitly dependent on ζ in Eq. (7). We find

$$i\frac{\partial \boldsymbol{u}}{\partial \zeta} = -\frac{\Gamma_0}{2}\boldsymbol{\sigma}_2 \cdot \boldsymbol{u}. \tag{8}$$

The eigenvectors of Eq. (8) are the two circular polarizations, with an accumulated phase of $\pm\pi\Gamma_0$ over one single birefringence length Λ. The theory agrees with the numerical results shown in Figs. 3 and 4 once we realize that the discrepancy from circular polarization is due to the terms depending explicitly on ζ in a periodic manner.

In a more formal way, the quasimodes of the Floquet-like vectorial equation (7) are investigated by expanding the solution as a Bloch wave [30]

$$\boldsymbol{u}(\zeta) = e^{i\beta\zeta}\sum_m \boldsymbol{u}_m e^{im\zeta}. \tag{9}$$

The corresponding eigenvalue problem in the rotated framework for small anisotropies and in the paraxial limit reads

$$\beta\boldsymbol{u}_m = -m\boldsymbol{u}_m + \frac{\Gamma_0}{4}[2\boldsymbol{\sigma}_2\boldsymbol{u}_m + (\boldsymbol{\sigma}_2 - i\boldsymbol{\sigma}_1)\boldsymbol{u}_{m-2} + (\boldsymbol{\sigma}_2 + i\boldsymbol{\sigma}_1)\boldsymbol{u}_{m+2}]. \tag{10}$$

According to Eq. (10), for small Γ_0 the quasimodes are circularly polarized with a phase $\Delta\varphi_{\text{geo}} = 2\pi\beta = \pm\pi\Gamma_0$ [Eq. (10) provides $\beta = \pm\Gamma_0/2$], the sign being determined by the handedness of the CP wave (i.e., the photon spin). This is in agreement with the numerical results plotted in Fig. 3(b) for Γ_0 up to 50°. The polarization of $\boldsymbol{u}$ is constant in propagation only in the rotated framework: when the transformation back to the laboratory framework is carried out, the CP will be retained only at the beginning and at the end of a birefringence length, whereas the Stokes vector will evolve periodically. As shown in Fig. 10 in Appendix A, S_3 versus ζ remains sinusoidal in this limit, whereas S_2 follows sinusoidal curves which are flattened around $z = \Lambda/4$ and $z = (3/4)\Lambda$, with a corresponding increase in $|S_1|$ in the same regions. This is confirmed for Γ_0 up to 50° by the exact evolution along z of the polarization plotted in Fig. 4. An additional effect observed in the numerical solution is that the value of S_1 in $z = 0$ is not vanishing, see Figs. 3(a) and 4(a). This can be explained from Eq. (10) once the terms $u_{\pm 1}$ are accounted for, see Appendix A. Even in this limit, the associated eigenvalue β (i.e., the local optical delay $\Delta\varphi_{\text{geo}}$) remains unperturbed, in accordance with the full simulations for $\Gamma_0 < 50°$. The higher-order harmonics u_m ($|m| > 1$) become relevant when $\Gamma_0 > 50°$, as witnessed by a strong deformation in S_3 versus z, see Fig. 4(c). Finally, Fig. 4(d) shows how only the average value of S_1 is different from zero, whereas S_2 and S_3 conserve a periodic motion with a vanishing average.

C. Coupling with diffraction

The terms on the RHS of Eq. (5) stem from the Laplacian operator, i.e., they originate from the natural spreading of light in space. In the case of twisted anisotropic materials, complicated effects arise from the coupling between neighboring points in the transverse plane. Indeed, a wave of a given linear polarization can solely correspond to a local eigensolution (extraordinary or ordinary polarized) of Maxwell's equations. Diffraction transports a portion of this local eigensolution to adjacent regions where the optic axis is differently oriented, in turn leading to a continuous local change in the beam polarization and phase. In agreement with the case of plane waves discussed in the previous section, a localized solution of the electromagnetic equation in this geometry needs to be periodic along z. The purpose of the current section is to find a simplified equation for the continuous component of the optical field using the normalized coordinates $\zeta = k_0\Delta n z$ and $\eta = x/\lambda$. In the equation for the paraxial field $\boldsymbol{u}$ in the rotated system [Eq. (5)] explicit terms from the imaginary unit can be found. Accounting solely for the continuous wave (cw) component in the rotated system, such a term can be canceled

out in the limit $\gamma = \Delta n/\bar{n} \ll 1$ by means of an additional z-independent gauge transformation (the detailed computation can be found in Appendix C). The new field $\boldsymbol{v}$ is defined by the transformation

$$\boldsymbol{u} = e^{i\boldsymbol{\sigma}_1\Gamma(x)/2} \cdot \boldsymbol{v}, \tag{11}$$

i.e., a complex phase term equal to $\Gamma(x)/2$. The proportionality factor 0.5 comes from the average of a sine square, the latter stemming from the polarization rotation due to the anisotropy multiplied by the externally imposed longitudinal sinusoidal modulation. Remarkably, the gauge transformation (11) appears only in the presence of diffraction, i.e., the interaction between light propagating in different positions x is accounted for. After writing the Fourier series $\boldsymbol{v}(\zeta) = \sum_m \boldsymbol{v}_m e^{im\zeta}$ with v_m being a slowly varying envelope with respect to ζ, the cw component of the field $\boldsymbol{v}_0$ satisfies the following Pauli-like equation (see Appendix D):

$$i\gamma\frac{\partial \boldsymbol{v}_0}{\partial\zeta} = -\frac{1}{8\pi^2\bar{n}^2}\frac{\partial^2\boldsymbol{v}_0}{\partial\eta^2} - \frac{\gamma\Gamma}{2}\left[\cos\left(\frac{\Gamma}{2}\right)\boldsymbol{\sigma}_2 + \sin\left(\frac{\Gamma}{2}\right)\boldsymbol{\sigma}_3\right]\cdot\boldsymbol{v}_0 + \frac{1}{32\pi^2\bar{n}^2}\left(\frac{\partial\Gamma}{\partial\eta}\right)^2\boldsymbol{v}_0. \tag{12}$$

The right-hand side of Eq. (8) is transformed to the term contained in the square brackets in Eq. (12). As a matter of fact, the gauge transformation expressed by Eq. (11) modifies the spin-orbit coupling due to the multiplication between the original operator $\boldsymbol{\sigma}_2$ and the gauge operator $e^{i\boldsymbol{\sigma}_1\Gamma(x)/2}$, in turn introducing a term containing $\boldsymbol{\sigma}_3$ proportional to $\sin(\Gamma/2)$. The spin-dependent phase modulation proportional to the local amplitude of the rotation angle $\Gamma(x)$ demonstrated with the plane-wave model [see Fig. 3(b)] is thus still at work [19], but with an additional rotation of the polarization related with the finite size of the structure. The Stokes vector of the resulting structured beams in the rotated framework shows a nonvanishing component S_1, beyond the dominant circular polarization component given by S_3. This effect is superposed to the nonvanishing S_1 predicted by Eq. (7) in the plane-wave limit and plotted in Fig. 3. Finally, the ratio between the two components of the Stokes vector also varies along the beam cross section.

To conclude this section, we discuss the effect of the gauge transformation given by Eq. (11) on the polarization of the quasimodes. The cw component in the rotated framework reads

$$\boldsymbol{u}_0 = \cos\left(\frac{\Gamma}{2}\right)\boldsymbol{v}_0 + i\sin\left(\frac{\Gamma}{2}\right)\boldsymbol{\sigma}_1\cdot\boldsymbol{v}_0. \tag{13}$$

According to Eq. (13), the polarization of a portion of the quasimode [proportional to $\cos(\frac{\Gamma}{2})$] found from Eq. (12) remains unvaried after the gauge transformation. On the other side, the remaining part proportional to $\sin(\frac{\Gamma}{2})$ is subject to a flip of its spin, i.e., the sign of the Stokes vector is inverted. The inversion occurs with eigenvalues $\pm i$ for the CP $\hat{x}' \pm i\hat{y}'$, respectively. When v_0 is CP (i.e., in the presence of a quasimode), the corresponding polarization of $\boldsymbol{u}_0$ strongly depends on the value of Γ. For $\Gamma = 90°$, the two contributions have the same weight, but encompassing a phase difference of 0 or π, according to which eigenvalue is considered. The corresponding overall polarization is thus linearly polarized along the vertical or the horizontal direction. For other values of Γ the polarization is instead elliptical. Finally, for small Γ Eq. (13) becomes $\boldsymbol{u}_0 \approx \boldsymbol{v}_0 + 0.5i\Gamma(x)\boldsymbol{\sigma}_1\cdot\boldsymbol{v}_0$.

III. NUMERICAL SIMULATIONS

We simulated the behavior of light in a twisted anisotropic material by using a combination of finite difference time domain (FDTD) and finite element method (FEM) software. For FDTD, we used the open-source code MEEP [31]. For FEM, we used the commercial software COMSOL Multiphysics® [32]. Both the numerical simulators solve the complete Maxwell equations, thus accounting for the full vectorial nature of the field and for light rays propagating at wide angles with respect to the main carrier propagating along z. Here in the main text we will present solely the results calculated with the FDTD code. Details of FDTD simulations are provided in Appendix E, whereas the comparison with FEM results is carried out in Appendix F.

A. Potential and quasimodes

As input condition for the numerical simulations, we do not consider a generic Gaussian profile, but we instead prefer the quasimode profile predicted in Ref. [19] using a simplified theoretical model. This approach allows us to directly address the validity range of the two models (i.e., the model in Ref. [19] and the one discussed in this paper) in describing PBP-based optical waveguides. To first approximation the quasimodes are CP modes subject to the following spin-dependent potential [19]:

$$V(x) = -\frac{S_3^{(0)}k_0\Delta n}{2}\Gamma(x) + \frac{1}{4\bar{n}k_0}\left[\left(\frac{\partial\Gamma}{\partial x}\right)^2 + k_0^2(\Delta n)^2\Gamma^2(x)\right]. \tag{14}$$

The quantity $S_3^{(0)}$ is the third Stokes parameter sampled at the beginning of the longitudinal sinusoidal oscillation. A shift of π in the sine (i.e., HWP longitudinal shift in real space) yields a change in sign in the first term, i.e., the photon spin corresponding to waveguiding is switched. Equation (14) is the effective potential once the light propagation is recast for the scalar field A in the form $i\partial_z A = -[1/(2\bar{n}k_0)]\partial_x^2 A + VA$. This means that light is attracted towards regions where V is lower, in agreement with the quantum-mechanical convention. The three terms composing the potential V have a simple physical interpretation. The first term comes from the net accumulation of PBP due to the periodic longitudinal rotation of the optic axis. The second term and the third terms are Kapitza-like terms proportional to the square of the gradient of the rotation angle θ [20]. Essentially, a periodic modulation of the phase generates a local modulation of the transverse wave vector k_x, in turn changing the equivalent kinetic energy due to its dependence on the square of k_x. In agreement with Eq. (12), the term depending on the longitudinal derivative is $O[(\Delta n)^2]$ and can be neglected in the adiabatic limit. In practice, for a fixed material the approximation will start to fail for large enough twisting angle, given that this phase term depends quadratically on Γ_0. Hereafter we set the wavelength to $\lambda = 1\mu$m and

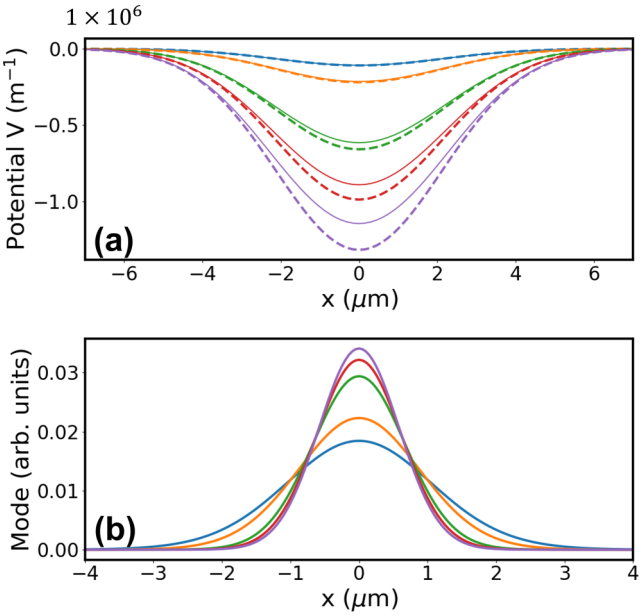

FIG. 5. Theoretical model in the limit of purely CP quasimodes. Photonic potential (a) V and (b) the corresponding fundamental mode (the intensity profile is shown) versus x. From shallower to deeper potential well (corresponding to a narrower fundamental mode), the maximum rotation angle Γ_0 is 10° (blue), 20° (orange), 60° (green), 90° (red), and 120° (magenta). In panel (a), solid and dashed lines correspond to the full potential evaluated from the entire Eq. (14) or only its first term, respectively.

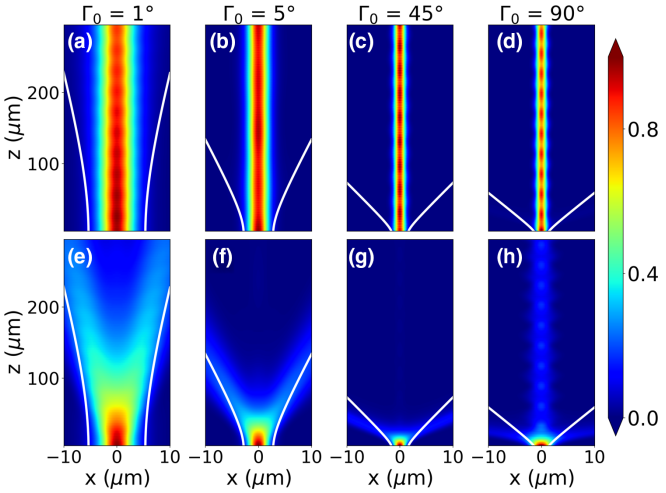

FIG. 6. Full numerical simulation of the light propagation for CP inputs of opposite helicity. Time-averaged intensity distribution calculated via FDTD simulations for (a)–(d) RCP and (e)–(h) LCP input polarization for $w_D = 3$ μm and increasing Γ_0 from left to right. The scalar eigenfunctions of the potential given by Eq. (14) are used as the transverse shape of the input. The white solid lines represent the spreading that would occur in the case of a homogeneous material. Finally, the anisotropic material starts in $z = 2$ μm.

the birefringence to $\Delta n = 0.2$. The longitudinal shape of the modulation is kept sinusoidal in the remainder of the paper. The transverse distribution of the optic axis is assumed to be Gaussian by setting $\Gamma(x) = \Gamma_0 \exp[-(x^2/w_D^2)]$. Figure 5 summarizes the behavior of the potential. The first term in Eq. (14) is the most important term, assuming a confining or a repelling nature according to the spin of the impinging wave. The term proportional to $(\partial_x \Gamma)^2$ takes a typical W shape and is negligible with respect to the other two terms for $w_D > 1$ μm. Finally, the term proportional to Γ^2 is intrinsically defocusing (i.e., a positive hump), achieving an amplitude of about 20% of the overall potential for $\Gamma_0 = 120°$. This is visible in Fig. 5(a), where the potential versus x for different Γ_0 is plotted.

To address the confinement strength of the photonic effective potential, the value of V can be transformed into an effective gradient in the refractive index δn. Recalling that $V \approx -2\bar{n}k_0\delta n$, we obtain for example $\delta n \approx 0.05$ for $V = 1 \times 10^6$ m^{-1}. In Fig. 5(b) the corresponding fundamental quasimode width versus x for several Γ_0 is shown. In our case the beam width—defined as $w = 2[\int x^2 I(x)dx / \int I(x)dx]^{1/2}$—spans from 5.4 μm at $\Gamma_0 = 1°$ to 1.3 μm at $\Gamma_0 = 90°$.

B. Propagation of quasimodes

At the entrance of the twisted material we used the quasimode calculated from Eq. (14) (see Appendix E for the employed procedure). A survey of the intensity distribution versus the twisting angle Γ_0 is provided in Fig. 6. In agreement with the strong spin-orbit coupling of our system, the general behavior for Γ_0 lower than 90° strongly depends on the wave handedness: RCP (right CP) undergoes a net confinement while propagating [Figs. 6(a)–6(d) shows the case $w_D = 3$ μm; additional simulations not shown here demonstrate that an analogous behavior is found for larger w_D], whereas the LCP (left CP) waves spread more than would occur in a homogeneous cell, see Figs. 6(e)–6(h). In each panel the white solid lines show the corresponding unconstrained diffraction (width $1/e^2$). With reference to the confined case, the quasimodes are a very good approximation: the envelope of the beam propagates with very small oscillations for Γ_0 up to 90°. At these large angles, the trapping is retained, but the observed breathing amplitude is quite large. Indeed, at large Γ_0 a new propagation regime arises: the optical propagation does not significantly depend anymore on the input helicity. A precursor of this behavior is already visible in Fig. 6(h), where at $\Gamma_0 = 90°$ an appreciable portion of the input power is guided, even for the polarization where defocusing takes place for lower angles. This behavior is in remarkable agreement with the plane-wave model plotted in Fig. 3, where the accumulation of PBP stops to monotonically increase for $\Gamma_0 > 110°$. The dependence of the power coupled to the quasimode versus Γ_0 and the input polarization is plotted in Fig. 7. For small angles the whole system response is analogous to a circular birefringent material [see Fig. 7(a)], where the confinement and defocusing of the beam depends on the handedness at the input. This is similar to what happens in cholesteric liquid crystals, where a helically twisted uniaxial behaves at large scales like a circularly birefringent material [23]. The two curves for different spins starts to flex towards each other around $\Gamma_0 \approx 50°$, eventually crossing in $\Gamma_0 = 120°$. Figure 7(b) shows the guided power when the input polarization is linearly polarized. At small rotations the behavior is almost polarization-independent, in agreement

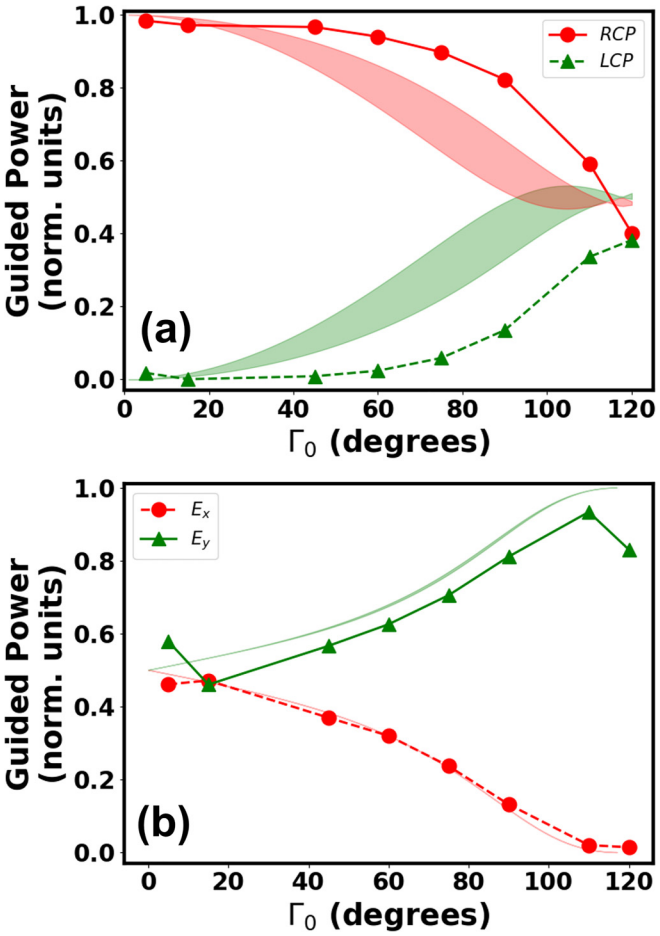

FIG. 7. Effects of the gauge transformation on the polarization of the guided quasimodes. Power coupled to the Berry waveguide for input (a) circular, and (b) linear vertical and horizontal polarizations versus the maximum rotation angle Γ_0. Symbols are values extrapolated from the FDTD simulations, whereas the shaded regions are the theoretical predictions from Eq. (13). Theoretical predictions corresponds to a surface because we are considering a range for the possible width of the quasimode, see the main text. The waveguide parameters are the same as for Fig. 6. The guided power is measured in $z = 200$ μm by integrating the intensity around the origin $x = 0$ on a window of overall size 10 μm.

with Fig. 7(a). As the twisting gets larger the two curves diverge from each other in a symmetric way. Stated otherwise, the degeneracy between the vertical (parallel to y) and the horizontal (parallel to x) polarization is broken. Around $\Gamma_0 = 120^\circ$ the optimal coupling to the quasimode occurs for the vertical polarization, whereas the orthogonal polarization reaches its maximum broadening due to the presence of a repelling potential. The general trend of the FDTD simulations (lines with symbols in Fig. 7) is in qualitative agreement with the plane-wave model developed in Sec. II B and with the gauge transformation Eq. (13) (shaded regions in the same figure). In other words, the quasimodes are no more CP because (i) a linear polarization component emerges due to the longitudinal simulations, even in the plane-wave limit; and (ii) the polarization dependence of the guiding effect strongly depends on the twisting angle due to the local gauge transformation, or, in more physical terms, due to the strong transverse coupling between regions with different twisting, ultimately induced by the natural tendency of light to diffract.

For the sake of quantitative comparison, on the theoretical side we compute the overlap integral between a nonstructured input beam and the quasimode in a simplified manner. We take a given Gaussian beam at the input, with an x-independent polarization, selected as indicated by the legends in Fig. 7. To find an approximation for the structured localized mode, the transformation given by Eq. (13) is then applied to this beam (i.e., the latter is $\boldsymbol{v}_0$ in this case), but with a polarization given by the plane-wave model computed for each value of Γ_0, see Fig. 3. The final step is to compute the overlap between the two spinors. We stress that, (i) to account for the variations in the width of the quasimode versus Γ_0 (see Fig. 5), we consider two different widths for the quasimode: 1 and 5 μm, corresponding to the edges of the shaded region; (ii) the exact $\boldsymbol{v}_0$ is already a structured beam, whereas here its polarization is taken to be invariant through its cross section.

C. Full characterization in terms of Stokes parameters

A deeper understanding on the physical mechanism behind the light confinement is achieved when the Stokes parameters of the propagating beams are plotted. Figures 8 and 9 show the Stokes parameters corresponding to the trapped beam plotted in Figs. 6(a)–6(d). The Stokes parameters are shown in proximity of the input interface (Fig. 8) and deep inside the waveguide (Fig. 9) to show the effects of the mode coupling and the stationary localized wave, respectively. For very small angles ($\Gamma_0 = 1^\circ$), the mode computed from Eq. (14) describes very well the propagating quasimode: the two Stokes parameters S_2 and S_3 vary sinusoidally with a period given by Λ and a relative shift of a quarter of period, $\Lambda/4$, whereas S_1 is negligibly small. For $\Gamma_0 = 5^\circ$ the situation is very similar, except for the appearance of a nonvanishing S_1, in accordance with Fig. 3(a). For $\Gamma_0 = 45^\circ$ a discrepancy in the polarization at the input interface is observed, with the emission of polarized radiation modes. In the bulk the sinusoidal variation of S_2 and S_3 is observed, but, unlike for smaller angles, S_1 is quite large, and encompasses a large z-invariant value superposed with a smaller sinusoidal oscillation of period Λ. For $\Gamma_0 = 90^\circ$ the coupling gets worse, with the periodicity being lost near the input interface. The oscillatory behavior of S_2 and S_3 is recovered into the bulk, although now the dominant component is S_1, the latter behaving similar to what is predicted by the plane-wave model plotted in Fig. 4(a). A large (about 180°) phase shift of the longitudinal oscillation between the center and the tails of the guided mode is observed for all the three Stokes parameters, even when the stationary regime is achieved: the quasimode is thus structured even along the transverse direction. The described dynamics confirms that the polarization of the quasimode follows at least qualitatively Eq. (13), and that the plane-wave approach to calculate the phase delay shown in Fig. 3(b) is quite reliable even in the presence of a local twisting. We thus evince that the breathing behavior observed in the intensity profile (Fig. 6) is due to a mismatch between the approximated quasimode (pseudoscalar) and the real mode, the latter being highly structured both along the longitudinal and the transverse direction.

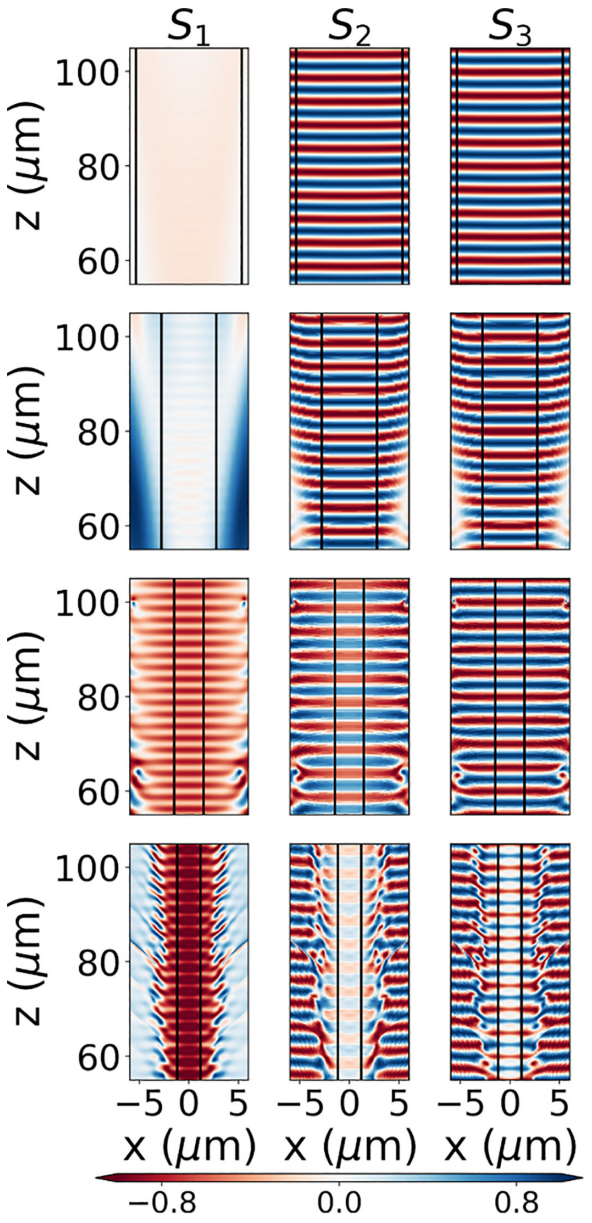

FIG. 8. Polarization transient at the input interface. Stokes parameters nearby the input interface extracted from FDTD simulations, plotted for $\Gamma_0 = 1^\circ$, 5°, 45°, and 90° from top to bottom, respectively. The input is a RCP mode with shape found from the potential (14).

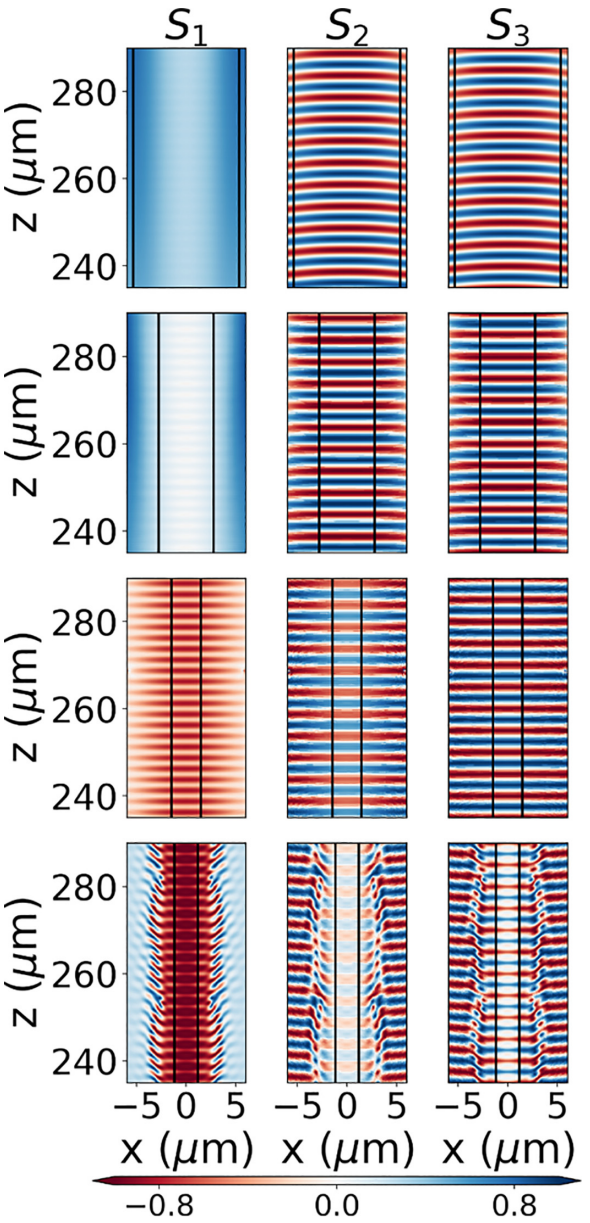

FIG. 9. Stationary distribution for the polarization state of the quasimode. Parameters are the same of Fig. 8, but at the end of the numerical grid, i.e., for $z > 250$ μm.

IV. SUMMARY OF THE MAIN RESULTS

This work contains the following main results:

(1) In a transversely invariant but longitudinally rotated anisotropic material subject to a finite gradient in the twisting angle, it is possible to control all the Stokes parameters using a sample length corresponding to the full wave plate (FWP), see Figs. 3 and 4. Indeed, a tunable amount of S_1 can be achieved by changing the amplitude of the local modulation. A nonvanishing S_2 can be finally arranged by a constant relative rotation of the optic axis [i.e., by rotating the whole Poincaré sphere in Fig. 3(c)]. To confirm this numerical result theoretically, we found a new vectorial paraxial equation [Eq. (6)] by an exact power expansion in the medium normalized anisotropy $\gamma = \Delta n/\overline{n}$. Periodic solutions in terms of Floquet series confirm that the quasimodes are circularly polarized for small rotations, but with an increasing S_1 as rotation gets larger [see Eq. (10)]. The eigenvalue stays unperturbed for small rotations, thus showing that the first and main term in the photonic potential given by Eq. (14) remains valid in this limit.

(2) As a direct consequence of the previous point, the quasimode of a Berry waveguide featuring a finite longitudinal gradient cannot be purely circularly polarized. In particular, a constant component S_1 appears as the rotation is increased, a fact confirmed by the full numerical simulations of the Maxwell's equations. Moreover, the exact polarization of the quasimode will vary along the cross section, thus providing a full structured beam both along the transversal and the longitudinal direction.

(3) The transverse coupling due to diffraction in a transversely inhomogeneous twisted sample can be modeled using point-dependent gauge transformations. This, in turn, yields the appearance of a Kapitza potential proportional to the transverse gradient of the twist [see the last term in Eq. (12)], and of a point-dependent rotation of the polarization, see Eq. (13). This is another factor making the quasimode a fully structured beam [33], even in the transverse plane. In particular, the gauge transformation directly modifies the local change in polarization, see the term between square brackets in Eq. (12). Incidentally, such a term survives even in the case of square-wave modulation along the longitudinal direction for the rotation angle θ, where the path of the polarization eigenmodes always crosses the two poles in the plane-wave limit. Accordingly, in the numerical simulations the polarization of the localized wave is transversely variant, and the coupling between circularly polarized inputs and the quasimodes drastically changes as the twisting ramps up.

(4) Both the plane-wave model and the gauge transformation predict that the average polarization of the quasimode in the rotated paraxial framework tends to become linearly polarized as the rotation angle increases. This is numerically confirmed by the emergence of a guided mode even when the CP at the input has a helicity corresponding to a defocusing potential according to Eq. (14), see Fig. 6(h). This behavior was erroneously attributed by some of us to the Kapitza effect in the Supplemental Material of Ref. [19].

(5) Despite the changes in the polarization described in the previous points, the mode profile calculated by solving the scalar equation with the potential given by Eq. (14) provides a very good approximation for intensity profile of the fundamental quasimode, for angles in our case up to 90°. This is the first time that such a quantitative comparison is carried out, given that in Ref. [19] we used only Gaussian beams of fixed width as input fields. We also showed that the transverse Kapitza potential is negligible, if subwavelength twisting of the material is left out: from Fig. 5, the interplay between the accumulated PBP and the longitudinal Kapitza effect determines the light propagation. Given that the Kapitza term is quadratic in the rotation angle, the PBP dominates at low angles, whereas the defocusing contribution of the Kapitza term becomes more and more relevant as the rotation is increased.

(6) For very large rotation angles, several new effects come into play. Even in the adiabatic limit (small anisotropy Δn), the accumulated PBP is no more monotonic [see Fig. 3(b)] given that the polarization path on the Poincaré sphere strongly differs from simple circles already in the plane-wave limit, see Fig. 3(c). The real propagation is indeed way more complex than Eq. (6), as several new terms proportional to γ^2 and higher powers of γ provide a non-negligible contribution owing to the faster changes in the polarization, see Appendix A. This means that the first term in the photonic potential given by Eq. (14) is wrong in this limit, a limitation not found in Ref. [19]. To mention only a single effect related to fast variations in the polarization, in the adiabatic limit governed by Eq. (7) the longitudinal Kapitza effect is evidently absent, see also the results based upon the Jones formalism plotted in Fig. 3(b).

V. CONCLUSIONS

In this paper we investigated theoretically and numerically the waveguiding observed in a periodically twisted anisotropic material and based upon a transverse gradient in the Pancharatnam-Berry phase. With respect to our previous work, we improved the theory by accounting for higher-order effects by implementing a combination of plane-wave models and gauge transformations. The model clearly shows that the guided modes feature a point-dependent polarization even across the transverse plane. For small angles, a purely circular polarized beam in the rotated paraxial framework approximates well the confined mode, the transverse shape of the beam being in good agreement with the scalar potential originating from the PBP. For larger rotations, all the three Stokes parameters (including S_1) are not vanishing, in disagreement with the intuitive picture based upon a plane wave in the presence of a longitudinal modulation in the form of a square wave. Furthermore, as the rotation increases the helicity of the quasimode starts to flip and the mode to be strongly structured along its cross section.

Although already observed in the nonlinear regime [22], the experimental realization of continuous PBP waveguides in the linear regime is the next step: different approaches to achieve this aim are currently pursued, including photopolymerization of liquid crystals [12,34,35], multistack of inhomogeneously rotated liquid crystals plates [36], and femtosecond writing of transparent materials [37]. As pinpointed in this article, these waveguides would support structured modes [38], thus representing an important advance in the current research about multimodal optical communications [33,39], both in the classical [40] and in the quantum regime [41]. In a broader physical perspective, our paper confirms a strict relation between twisted anisotropic media and propagation of charged particles in a magnetic field, proposing this optical platform as a promising candidate for the theoretical and experimental investigation of gauge-related and spin-orbit effects in an optical system [42–49].

ACKNOWLEDGMENTS

C.P.J. has received funding from the European Union's Framework Programme for Research and Innovation Horizon 2020 under the Marie Sklowdowska-Curie Grant Agreement No. 889525. S.V.A. is part of the Max Planck School of Photonics supported by BMBF, Max Planck Society, and Fraunhofer Society. This work is supported by the DFG Collaborative Research Center "NOA—Nonlinear Optics down to Atomic scales," Grant No. SFB 1375. The computational experiments were performed on resources of Friedrich Schiller University Jena supported in part by DFG Grants No. INST 275/334-1 FUGG and No. INST 275/363-1 FUGG.

APPENDIX A: PLANE-WAVE PROPAGATION IN LONGITUDINALLY TWISTED MATERIALS

We first apply the slowly varying envelope approximation (SVEA) to Eq. (5) by setting $\boldsymbol{\psi}' = e^{ik_0 N z} \cdot \boldsymbol{u}$, where $\boldsymbol{N} =$

$(n_\perp, 0; 0, n_\parallel)$ [19]. We obtain

$$2ik_0\boldsymbol{N}\cdot e^{ik_0Nz}\cdot\frac{\partial\boldsymbol{u}}{\partial z} - i\boldsymbol{\sigma_2}\cdot\left(2ik_0\frac{\partial\theta}{\partial z}\boldsymbol{N}\cdot e^{ik_0Nz}\cdot\boldsymbol{u}+\frac{\partial^2\theta}{\partial z^2}e^{ik_0Nz}\cdot\boldsymbol{u}\right) - \left(\frac{\partial\theta}{\partial z}\right)^2 e^{ik_0Nz}\cdot\boldsymbol{u}=0. \tag{A1}$$

After multiplying both the sides of Eq. (A1) by e^{-ik_0Nz}, we find that

$$2ik_0\boldsymbol{N}\cdot\frac{\partial\boldsymbol{u}}{\partial z}+2k_0\frac{\partial\theta}{\partial z}\tilde{\sigma}_2(z)\cdot\boldsymbol{N}\cdot\boldsymbol{u}-i\frac{\partial^2\theta}{\partial z^2}\tilde{\sigma}_2(z)\cdot\boldsymbol{u} - \left(\frac{\partial\theta}{\partial z}\right)^2\cdot\boldsymbol{u}=0, \tag{A2}$$

where

$$\tilde{\sigma}_2(z)=\cos(k_0\Delta nz)\boldsymbol{\sigma}_2+\sin(k_0\Delta nz)\boldsymbol{\sigma}_1. \tag{A3}$$

$\tilde{\sigma}_2$ oscillates along z with the same period given by the material birefringence. We want to express Eq. (A2) solely in terms of Pauli matrices. At this purpose we set $\boldsymbol{N}=\bar{n}\boldsymbol{I}-\frac{\Delta n}{2}\boldsymbol{\sigma}_3$, where $\bar{n}=(n_\perp+n_\parallel)/2$ is the refractive index perceived by a circular polarization. Direct substitution into Eq. (A2) yields

$$2ik_0\left(\bar{n}\boldsymbol{I}-\frac{\Delta n}{2}\boldsymbol{\sigma}_3\right)\cdot\frac{\partial\boldsymbol{u}}{\partial z}+2k_0\frac{\partial\theta}{\partial z}[F(z)\boldsymbol{\sigma}_2+G(z)\boldsymbol{\sigma}_1]\cdot\boldsymbol{u} - i\frac{\partial^2\theta}{\partial z^2}[\cos(k_0\Delta nz)\boldsymbol{\sigma}_2+\sin(k_0\Delta nz)\boldsymbol{\sigma}_1]\cdot\boldsymbol{u} - \left(\frac{\partial\theta}{\partial z}\right)^2\boldsymbol{u}=0, \tag{A4}$$

where we introduced $F(z)=\bar{n}\cos(k_0\Delta nz)+i\frac{\Delta n}{2}\sin(k_0\Delta nz)$ and $G(z)=\bar{n}\sin(k_0\Delta nz)-i\frac{\Delta n}{2}\cos(k_0\Delta nz)$. We are interested in the resonant case when the external modulation given by $\theta(z)$ is synchronized with the natural oscillation of the polarization setting $\Lambda=\lambda/\Delta n$. From Eq. (A4) this corresponds to a continuous-wave component coming from the terms depending on $\theta(z)$. The inversion operator of the matrix factor in front of $\partial_z\boldsymbol{u}$ is

$$\left(\bar{n}\boldsymbol{I}-\frac{\Delta n}{2}\boldsymbol{\sigma}_3\right)^{-1}=\frac{1}{\bar{n}}\frac{1}{1-\left(\frac{\Delta n}{2\bar{n}}\right)^2}\left(\boldsymbol{I}+\frac{\Delta n}{2\bar{n}}\boldsymbol{\sigma}_3\right). \tag{A5}$$

Applying the inversion operator (A5) to (A4) we find

$$2ik_0\bar{n}\frac{\partial\boldsymbol{u}}{\partial z}+K\left(\boldsymbol{I}+\frac{\Delta n}{2\bar{n}}\boldsymbol{\sigma}_3\right)\left[X\boldsymbol{\sigma}_2+Y\boldsymbol{\sigma}_1-\left(\frac{\partial\theta}{\partial z}\right)^2\right]\cdot\boldsymbol{u}=0, \tag{A6}$$

where we set

$$X=2k_0\frac{\partial\theta}{\partial z}F(z)-i\frac{\partial^2\theta}{\partial z^2}\cos(k_0\Delta nz), \tag{A7}$$

$$Y=2k_0\frac{\partial\theta}{\partial z}G(z)-i\frac{\partial^2\theta}{\partial z^2}\sin(k_0\Delta nz), \tag{A8}$$

$$K=[1-(\gamma/2)^2]^{-1}. \tag{A9}$$

For the sake of compactness, we introduce the normalized anisotropy $\gamma=\Delta n/\bar{n}$. Computation of the operator multiplication in Eq. (A6) yields

$$i\frac{\partial\boldsymbol{u}}{\partial z}=K\frac{i(\gamma/2)X-Y}{2k_0\bar{n}}\boldsymbol{\sigma}_1\cdot\boldsymbol{u}-K\frac{X+i(\gamma/2)Y}{2k_0\bar{n}}\boldsymbol{\sigma}_2\cdot\boldsymbol{u} + \frac{K}{2k_0\bar{n}}\left(\boldsymbol{I}+\frac{\gamma}{2}\boldsymbol{\sigma}_3\right)\left(\frac{\partial\theta}{\partial z}\right)^2\cdot\boldsymbol{u}. \tag{A10}$$

By expanding K in a power series of the normalized anisotropy γ, Eq. (A10) can be recast as a power series of γ itself. Before doing that, it is convenient to introduce the phase retardation $\zeta=k_0\Delta nz$, i.e., to normalize the propagation distance with respect to the natural rotation of the polarization vector. Equations (A7)–(A9) can then be expressed as a quadratic polynomial in γ:

$$\frac{X}{\bar{n}^2}=k_0^2[a_X(\theta)\gamma+b_X(\theta)\gamma^2], \tag{A11}$$

$$\frac{Y}{\bar{n}^2}=k_0^2[a_Y(\theta)\gamma+b_Y(\theta)\gamma^2], \tag{A12}$$

$$K\approx 1+\left(\frac{\gamma}{2}\right)^2. \tag{A13}$$

The new terms defined in the above equations are

$$a_X(\zeta,\theta)=2\cos\zeta\frac{\partial\theta}{\partial\zeta}, \tag{A14}$$

$$b_X(\zeta,\theta)=i\left(\sin\zeta\frac{\partial\theta}{\partial\zeta}-\cos\zeta\frac{\partial^2\theta}{\partial\zeta^2}\right), \tag{A15}$$

$$a_Y(\zeta,\theta)=2\sin\zeta\frac{\partial\theta}{\partial\zeta}, \tag{A16}$$

$$b_Y(\zeta,\theta)=-i\left(\cos\zeta\frac{\partial\theta}{\partial\zeta}+\sin\zeta\frac{\partial^2\theta}{\partial\zeta^2}\right). \tag{A17}$$

Next we expand Eq. (A10) in a power series of γ, halting the series at the linear order. Equation (A10) then yields

$$i\frac{\partial\boldsymbol{u}}{\partial\zeta}=-\frac{1}{2}(a_Y\boldsymbol{\sigma}_1+a_X\boldsymbol{\sigma}_2)\cdot\boldsymbol{u}+\frac{\gamma}{2}\left[\left(\frac{ia_X}{2}-b_Y\right)\boldsymbol{\sigma}_1 - \left(\frac{ia_Y}{2}+b_X\right)\boldsymbol{\sigma}_2+\left(\frac{\partial\theta}{\partial\zeta}\right)^2\right]\cdot\boldsymbol{u}. \tag{A18}$$

Using Eqs. (A14) and (A16), for small values of the anisotropy Eq. (A18) turns into

$$i\frac{\partial\boldsymbol{u}}{\partial\zeta}=-\frac{\partial\theta}{\partial\zeta}[\sin(\zeta)\boldsymbol{\sigma}_1+\cos(\zeta)\boldsymbol{\sigma}_2]\cdot\boldsymbol{u}. \tag{A19}$$

We now consider the resonant case, where the optic axis is periodically modulated with a period equal to $\lambda/\Delta n$ in the real space. Thus, after taking a sinusoidal oscillation in the form $\theta(\zeta)=\Gamma_0\sin(\zeta)$, we find

$$i\frac{\partial\boldsymbol{u}}{\partial\zeta}=-\frac{\Gamma_0}{2}[\sin 2\zeta\ \boldsymbol{\sigma}_1+(1+\cos 2\zeta)\boldsymbol{\sigma}_2]\cdot\boldsymbol{u}. \tag{A20}$$

From the Bloch-Floquet theorem, the quasimode can be expressed as

$$\boldsymbol{u}(\zeta)=e^{i\beta\zeta}\sum_m\boldsymbol{u}_m e^{im\zeta}, \tag{A21}$$

where β is the associated eigenvalue. Next step is inserting the ansatz Eq. (A21) into Eq. (A20). For each integer m the following relation is found:

$$\beta \boldsymbol{u}_m = -m\boldsymbol{u}_m + \frac{\Gamma_0}{4}[2\boldsymbol{\sigma}_2\boldsymbol{u}_m + (\boldsymbol{\sigma}_2 - i\boldsymbol{\sigma}_1)\boldsymbol{u}_{m-2} + (\boldsymbol{\sigma}_2 + i\boldsymbol{\sigma}_1)\boldsymbol{u}_{m+2}]. \tag{A22}$$

Equation (A22) shows that the components u_m of different parity (i.e., the terms u_m corresponding to m either even or odd) form two independent sets of values. In the case of small rotations (i.e., small Γ_0), the oscillations of the field amplitude are small, which means $\boldsymbol{u}_m \approx 0$ for $m \neq 0$. Equation (A22) then provides

$$\beta \boldsymbol{u}_0 = \frac{\Gamma_0}{2}\boldsymbol{\sigma}_2 \cdot \boldsymbol{u}_0. \tag{A23}$$

From the latter it is straightforward to find that the eigenvectors are the two CPs $|L\rangle$ and $|R\rangle$, with the associated eigenvalues $\beta = \pm\Gamma_0/2$. In the real-space coordinates, the phase delay acquired at each HWP length is $\pi\Gamma_0$, in agreement with the numerical simulations shown in Fig. 3.

At the next order, we have $u_{\pm 1} \neq 0$. In this case Eq. (A22) provides an additional eigenvalue equation

$$\Delta\beta\, \boldsymbol{u}_{\pm 1} = \left[\frac{\Gamma_0}{2}\boldsymbol{\sigma}_2 - (\beta_0 \pm 1)\boldsymbol{I}\right]\boldsymbol{u}_{\pm 1}, \tag{A24}$$

where we supposed $\beta \approx \beta_0 + \Delta\beta$, and where $\beta_0 = \Gamma_0/2$ is the eigenvalue at the lowest approximation order, as determined by Eq. (A23). The eigenvectors are still circularly polarized. The two eigenvalues are $\pm(\Gamma_0 + 1)$ and ± 1, respectively, the sign depending on the sign of m. The solutions $|\Delta\beta| = \Gamma_0 + 1$ are not acceptable because they are inconsistent with the full eigenvalue equation (A22). On the other side, solutions featuring $|\Delta\beta| = 1$ are acceptable because they imply a shift of 2π in the eigenvalue according to Eq. (A21), thus representing the same solution according to the ansatz expressed by Eq. (A23). Summarizing, the simultaneous solution of Eqs. (A23) and (A24) tells us that the beam at $z = 0$ is circularly polarized with an eigenvalue equal to β_0. An additional component with $|m| = 1$ is present, providing a small change in the beam polarization, even in the rotated framework. This latter oscillation is actually responsible for the nonvanishing S_1 even in $z = 0$, see Fig. 4(a). To conclude, we notice that this simplified approach does not allow us to quantify the relative weight of the two components $\boldsymbol{u}_0$ and $\boldsymbol{u}_{\pm 1}$, the latter evidently requiring the components $\boldsymbol{u}_m$ for $|m| > 1$ to be accounted for.

Figure 10(a) compares the Stokes parameters in the laboratory framework when only $\boldsymbol{u}_0$ is nonvanishing to the case where a $\boldsymbol{u}_1$ component with a 10% amplitude of $\boldsymbol{u}_0$ is present [Fig. 10(b)]. Comparison with the full numerical simulations is discussed in the main text in Sec. II B. To help the comparison, here we stress out the computation to connect the rotated and the laboratory framework. The wave function in the laboratory framework is linked to the coefficients $\boldsymbol{u}_m$ via

$$\boldsymbol{\psi} = e^{i\beta\zeta}e^{ik_0 n_\perp \zeta} \times \begin{pmatrix} \cos\theta \sum_m u_{x,m}e^{im\zeta} - \sin\theta \sum_m u_{y,m}e^{i(m+1)\zeta} \\ \sin\theta \sum_m u_{x,m}e^{im\zeta} + \cos\theta \sum_m u_{y,m}e^{i(m+1)\zeta} \end{pmatrix}. \tag{A25}$$

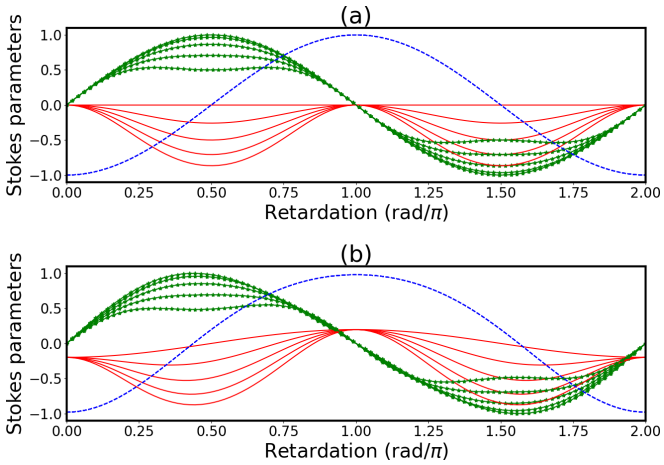

FIG. 10. (a) The Stokes parameters versus the phase retardation for a CP wave in the rotated framework rotated back to the laboratory frame. Only $\boldsymbol{u}_0$ is nonvanishing in this case. (b) Stokes parameters versus phase retardation when $\boldsymbol{u}_1 = -0.1\boldsymbol{u}_0$. In both panels the blue dashed curve is S_3, S_2 the green lines with symbol, S_1 the solid red lines. The values used for Γ_0 are 0°, 7.5°, 15°, 22.5°, 30°

In the limit of small angle $\theta = \Gamma_0 \sin\zeta$, considering only $\boldsymbol{u}_0 \neq 0$, we find

$$\boldsymbol{\psi}_0 \approx \begin{pmatrix} u_{x,0} \\ u_{y,0}e^{i\zeta} \end{pmatrix} + \frac{\Gamma}{2i}\begin{pmatrix} -u_{y,0}e^{i\zeta} \\ u_{x,0} \end{pmatrix}, \tag{A26}$$

where the common phase $(\beta + k_0 n_\perp)\zeta$ has been removed for the sake of clarity. For $\Gamma = 0$, the limit of a homogeneous wave plate is correctly retrieved. When considering the terms for $|m| = 1$ we obtain

$$\boldsymbol{\psi}_0 \approx \cdots + \begin{pmatrix} u_{x,1}e^{i\zeta} + u_{x,-1}e^{-i\zeta} \\ u_{y,1}e^{2i\zeta} + u_{y,-1} \end{pmatrix} + \frac{\Gamma}{2i}\begin{pmatrix} -u_{y,-1} - u_{y,1}e^{2i\zeta} \\ u_{x,-1}e^{-i\zeta} + u_{x,1}e^{i\zeta} \end{pmatrix}. \tag{A27}$$

The presence of terms not explicitly dependent on ζ demonstrates how the harmonics for $|m = 1|$ affect the average value of $\boldsymbol{\psi}_0$, in agreement with Fig. 10(b).

APPENDIX B: JONES MATRIX IN A LAYERED TWISTED MATERIAL

In the circular basis $(|L\rangle, |R\rangle)$ and for unidirectional light propagation, the Jones matrix for a transversely homogeneous slab of uniaxial material of thickness δ and twisted by an angle θ is

$$\boldsymbol{J}(\delta,\theta) = e^{i\bar{n}k_0\delta}\begin{pmatrix} \cos\left(\frac{k_0\Delta n\delta}{2}\right) & -i\sin\left(\frac{k_0\Delta n\delta}{2}\right)e^{2i\theta} \\ -i\sin\left(\frac{k_0\Delta n\delta}{2}\right)e^{-2i\theta} & \cos\left(\frac{k_0\Delta n\delta}{2}\right) \end{pmatrix} = e^{i\bar{n}k_0\delta}e^{-i\frac{k_0\Delta n\delta}{2}(\hat{s}\cdot\boldsymbol{\sigma})} = e^{i\bar{n}k_0\delta[1-\frac{\Delta n}{2\bar{n}}(\hat{s}\cdot\boldsymbol{\sigma})]}, \tag{B1}$$

where $\hat{s}(\theta) = \cos(2\theta)\hat{x} - \sin(2\theta)\hat{y}$. When the eigenvalues of the exponential matrix are computed, we correctly retrieve the ordinary and extraordinary plane waves as eigensolution of the system, but rotated by an angle θ with respect to the framework xy.

For a stack of infinitely thick layers of overall thickness L, the total transfer function is given by the multiplication of N

matrices $\boldsymbol{J}(\delta,\theta_m)$, each of them calculated in the limit $\delta\to 0$. This approach is valid in the limit of slow variations for the angle θ on the scale $\lambda/\Delta n$, i.e., in the adiabatic limit. Dubbing L the overall length of the twisted material, we have $\delta = L/N$; finally, in the limit of infinitely thin layers the transmission matrix in the absence of back-reflections is

$$\boldsymbol{J}_{\text{total}} = \lim_{N\to\infty}\prod_{m=1}^{N}\left[\boldsymbol{I} + ik_0\overline{n}\frac{L}{N}\begin{pmatrix}1 & -\frac{\gamma}{2}e^{2i\theta_m}\\ -\frac{\gamma}{2}e^{-2i\theta_m} & 1\end{pmatrix}\right]. \tag{B2}$$

From Eq. (B2) we deduce that the propagation of a plane wave in a longitudinally twisted geometry can be normalized with respect to the normalized anisotropy $\gamma = \Delta n/\overline{n}$.

The fundamental properties of the solutions to Eq. (B2) can be better visualized if we use the last expression in Eq. (B1). We find that

$$\boldsymbol{J}_{\text{total}} = e^{i\overline{n}k_0L}\lim_{N\to\infty}\prod_{m=1}^{N}e^{-i\frac{k_0\Delta n[\hat{s}(\theta_m)\cdot\boldsymbol{\sigma}]}{2}\frac{L}{N}}. \tag{B3}$$

According to Eq. (B3), if $\theta = \theta(\zeta)$ the optical propagation depends only on the phase retardation $k_0\Delta n\delta$, except for a phase term corresponding to the dynamic phase of a CP wave. Once $\boldsymbol{J}_{\text{total}}$ is known, the corresponding eigenmodes (i.e., the polarization at each full wave plate [FWP] distance) and the eigenvalues (i.e., the associated geometric phase) can be numerically computed using standard algebraic methods.

APPENDIX C: MODELLING OF THE TRANSVERSE COUPLING

We start by considering only the right-hand side (RHS) of Eq. (5); let us call it the operator $\hat{L}$. Applying the SVEA [see the definition of $\boldsymbol{u}$ before Eq. (A2) in Appendix A], we find

$$\hat{L} = -\frac{\partial^2\boldsymbol{u}}{\partial x^2} + \left(\frac{\partial\theta}{\partial x}\right)^2\boldsymbol{u} + i\frac{\partial^2\theta}{\partial x^2}\tilde{\boldsymbol{\sigma}}_2\cdot\boldsymbol{u} + 2i\frac{\partial\theta}{\partial x}\tilde{\boldsymbol{\sigma}}_2\cdot\frac{\partial\boldsymbol{u}}{\partial x}. \tag{C1}$$

The aim of the current section is to develop the transverse coupling alone, considering the minimal coupling with the evolution of the field along z. From Eq. (A4) we can use the simplified equation

$$2ik_0\left(\overline{n}\boldsymbol{I} - \frac{\Delta n}{2}\boldsymbol{\sigma}_3\right)\cdot\frac{\partial\boldsymbol{u}}{\partial z} = \hat{L}, \tag{C2}$$

i.e., we account only for the term providing the first derivative of the field along the propagation coordinate z. Application of the operator defined by Eq. (A5) to both sides provides

$$\begin{aligned}\frac{2ik_0\overline{n}}{K}\frac{\partial\boldsymbol{u}}{\partial z} &= \left(\boldsymbol{I} + \frac{\gamma}{2}\boldsymbol{\sigma}_3\right)\cdot\hat{Q}(x)\boldsymbol{u}\\ &+\left[\left(\boldsymbol{\sigma}_2 - \frac{i\gamma}{2}\boldsymbol{\sigma}_1\right)\cos(k_0\Delta nz)\right.\\ &\left.+\left(\boldsymbol{\sigma}_1 + \frac{i\gamma}{2}\boldsymbol{\sigma}_2\right)\sin(k_0\Delta nz)\right]\cdot\hat{P}(x)\boldsymbol{u},\end{aligned} \tag{C3}$$

where K has been defined in Eq. (A9) and

$$\hat{Q}(x) = -\frac{\partial^2}{\partial x^2} + \left(\frac{\partial\theta}{\partial x}\right)^2, \tag{C4}$$

$$\hat{P}(x) = i\frac{\partial^2\theta}{\partial x^2} + 2i\frac{\partial\theta}{\partial x}\frac{\partial}{\partial x}. \tag{C5}$$

Introducing the normalized transverse coordinate $\eta = x/\lambda$ and the retardation $\zeta = k_0\Delta nz$, Eq. (C3) can be recast as

$$i\gamma\frac{\partial\boldsymbol{u}}{\partial\zeta} = \frac{1}{8\pi^2\overline{n}^2}(\boldsymbol{T}_0 + \boldsymbol{T}_1\gamma + \boldsymbol{T}_2\gamma^2 + \cdots)\cdot\boldsymbol{u}. \tag{C6}$$

Until the order γ^2 we find

$$\boldsymbol{T}_0 = \hat{Q}(\eta)\boldsymbol{u} + [\boldsymbol{\sigma}_2\cos(\zeta) + \boldsymbol{\sigma}_1\sin(\zeta)]\hat{P}(\eta)\boldsymbol{u}, \tag{C7}$$

$$\boldsymbol{T}_1 = \frac{1}{2}\boldsymbol{\sigma}_3\cdot\hat{Q}(\eta)\boldsymbol{u} + \frac{i}{2}[\boldsymbol{\sigma}_2\sin(\zeta) - \boldsymbol{\sigma}_1\cos(\zeta)]\cdot\hat{P}(\eta)\boldsymbol{u}, \tag{C8}$$

$$\boldsymbol{T}_2 = \left(\frac{1}{2}\right)^2\boldsymbol{T}_0. \tag{C9}$$

Equation (C6) explicitly states that the effects of diffraction can be described as a power expansion in the normalized anisotropy γ. We finally take the resonant case setting $\theta(\eta,\zeta) = \Gamma(\eta)\sin(\zeta)$. At the lowest order in γ and considering only the averaged term along the propagation coordinate ζ, the field evolves according to

$$\begin{aligned}i\gamma\frac{\partial\boldsymbol{u}}{\partial\zeta} \approx \frac{1}{8\pi^2\overline{n}^2}&\left[-\frac{\partial^2\boldsymbol{u}}{\partial\eta^2} + \frac{1}{2}\left(\frac{\partial\Gamma}{\partial\eta}\right)^2\boldsymbol{u}\right.\\ &\left.+\frac{i\boldsymbol{\sigma}_1}{2}\cdot\left(\frac{\partial^2\Gamma}{\partial\eta^2}\boldsymbol{u} + 2\frac{\partial\Gamma}{\partial\eta}\frac{\partial\boldsymbol{u}}{\partial\eta}\right)\right].\end{aligned} \tag{C10}$$

The term proportional to $\boldsymbol{\sigma}_1$ can be eliminated by employing the gauge transformation $\boldsymbol{u} = e^{i\boldsymbol{\sigma}_1\Gamma/2}\cdot\boldsymbol{v}$, in turn providing the final result

$$i\gamma\frac{\partial\boldsymbol{v}}{\partial\zeta} \approx \frac{1}{8\pi^2\overline{n}^2}\left[-\frac{\partial^2\boldsymbol{v}}{\partial\eta^2} + \frac{1}{4}\left(\frac{\partial\Gamma}{\partial\eta}\right)^2\boldsymbol{v}\right]. \tag{C11}$$

APPENDIX D: DERIVATION OF THE COMPLETE MODEL

We can now derive the whole model for the optical propagation combining the results derived in Appendixes A and C. Joining Eqs. (C6) and (A19), in the normalized coordinate system $\eta\zeta$ we find

$$\begin{aligned}i\frac{\partial\boldsymbol{u}}{\partial\zeta} &= -\frac{\partial\theta}{\partial\zeta}[\sin(\zeta)\,\boldsymbol{\sigma}_1 + \cos(\zeta)\boldsymbol{\sigma}_2]\cdot\boldsymbol{u}\\ &+\frac{1}{8\pi^2\overline{n}^2\gamma}(\boldsymbol{T}_0 + \boldsymbol{T}_1\gamma + \boldsymbol{T}_2\gamma^2 + \cdots)\cdot\boldsymbol{u}.\end{aligned} \tag{D1}$$

In the limit of small anisotropy and in the resonant case $H(\zeta) = \sin(\zeta)$, Eq. (D1) provides

$$\begin{aligned}i\gamma\frac{\partial\boldsymbol{u}}{\partial\zeta} &= -\frac{\gamma\Gamma(\eta)}{2}\{\sin(2\zeta)\,\boldsymbol{\sigma}_1 + [1+\cos(2\zeta)]\boldsymbol{\sigma}_2\}\cdot\boldsymbol{u}\\ &+\frac{1}{8\pi^2\overline{n}^2}\left\{-\frac{\partial^2\boldsymbol{u}}{\partial\eta^2} + \frac{1}{2}\left(\frac{\partial\Gamma}{\partial\eta}\right)^2\boldsymbol{u} + \frac{i}{2}\{\sin(2\zeta)\,\boldsymbol{\sigma}_2\right.\\ &\left.+[1+\cos(2\zeta)]\boldsymbol{\sigma}_1\}\left(\frac{\partial^2\Gamma}{\partial\eta^2} + 2\frac{\partial\Gamma}{\partial\eta}\frac{\partial}{\partial\eta}\right)\boldsymbol{u}\right\}.\end{aligned} \tag{D2}$$

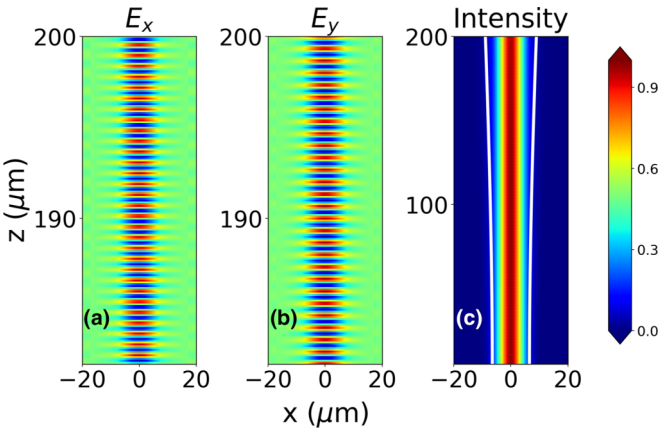

FIG. 11. Long FEM simulations for small rotation angles. Maps on the plane xz of the electric field components (a) E_x, (b) E_y, and (c) of the corresponding time-averaged Poynting vector component along the propagation distance z. A snapshot of the time-dependent electric fields for 180 μm $< z <$ 200 μm is shown in panels (a) and (b). The maximum rotation angle is $\Gamma_0 = 1^\circ$ and $w_D = 8$ μm. Input is a Gaussian of width 6.6 μm.

Equation (D2) describes the evolution of waves, including the beam variations occurring inside any single birefringence length. Equation (12) in the main text is then derived by rewriting the field as a Bloch wave and considering only the cw component. The last step is carried out in a simplified manner by averaging the ζ-dependent coefficients over a birefringence length. For a more accurate approach, see Eq. (A22). Finally, the terms explicitly dependent on i can be factored out by using a gauge transformation, in full analogy with what has been done to achieve Eq. (C11).

APPENDIX E: DETAILS OF THE FDTD IMPLEMENTATION

The FDTD is run using a continuous source with a wavelength of 1 μm. The switching parameters of the source are

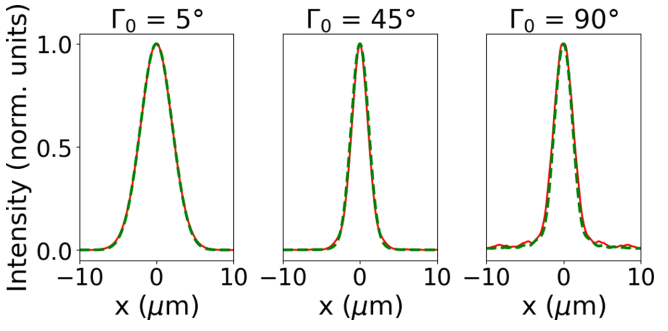

FIG. 12. Comparison of the output intensity profile computed with FDTD and FEM simulations. The normalized intensity cross section in $z = 50$ μm is plotted versus x for three different values of Γ_0, the latter being labeled at the top of each panel; the width of the twisting distribution is $w_D = 8$ μm. Solid red and green dashed lines correspond to FEM and FDTD, respectively. In both the simulators, the input is a circularly polarized Gaussian beam with a width equal to the effective fundamental mode.

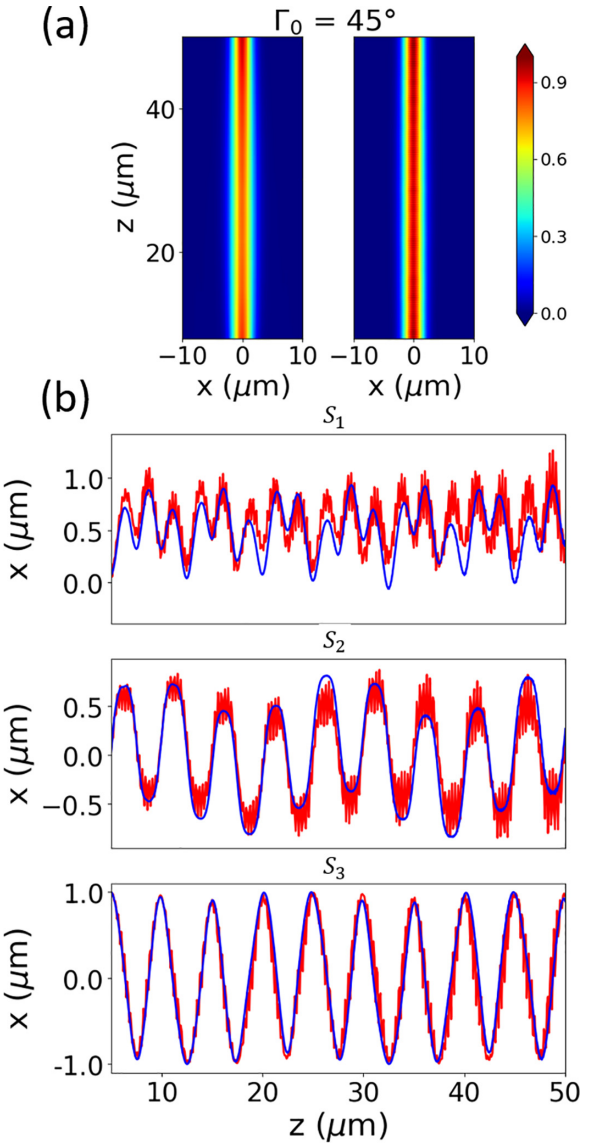

FIG. 13. Comparison of light evolution computed via FDTD and FEM simulations. (a) Intensity distribution for a Gaussian input of waist 2.4 μm over the plane x for $\Gamma_0 = 45^\circ$ and $w_D = 8$ μm, computed with FEM (left side) and FDTD (right side). (b) Corresponding evolution versus z of the Stokes parameters on the beam axis $x = 0$ μm; blue and red lines correspond to FDTD and FEM simulations, respectively.

chosen such that to achieve the stationary solutions inside the temporal duration of our simulations. To inject the quasimode as input on the FDTD simulations, we first generate a fictitious isotropic material with a refractive index profile matching the potential given by Eq. (14). The polarization is then transformed into circular by inserting a homogeneous layer of anisotropic material with thickness corresponding to a QWP. The dielectric permittivities of the QWP are taken identical to the twisted material to minimize the reflection at the input interface, the latter implying a change in the polarization actually transmitted into the structured material.

The time-average intensity is derived from the fields oscillating in time by either applying a low-pass Savitzky-Golay filter or by time averaging the electric field saved in one tem-

poral oscillation (21 points are saved in one oscillation) after the stationary regime is achieved. We verified that the two approaches yield the same results, with the first method presenting some small residual oscillation along the propagation direction. Analogously, the Stokes parameters are retrieved by deriving the complex amplitude of the field from the positions of the maxima in the temporal oscillation of the field. Notice that this procedure tacitly assumes a negligible amount of back-reflection in the twisted material. Also in this case, a more robust procedure based upon best fitting of the whole wave function along one period provides no substantial differences.

APPENDIX F: FEM SIMULATIONS AND COMPARISON WITH FDTD RESULTS

During our numerical efforts we found that FDTD simulations for very small angles (lower than 5°) do not converge properly, even with spatial steps of about 20 nm. In particular, the intensity profile and the two Stokes parameters S_2 and S_3 achieve a convergence, but the simulations predict a spurious S_1 component encompassing a nonvanishing error versus the coarseness of the numerical grid. Curiously, such a behavior does not take place for large angles. After several tests, we deduced that the error comes from the interpolation function used by the program to interpolate the given point-dependent function for the dielectric tensor, with the most critical point being the interface between the twisted material and the QWP layer. To verify the accuracy of the numerical results for small Γ_0, we used COMSOL Multiphysics® to simulate the light propagation, but using a Gaussian beam at the input, with a waist equal to the theoretical value predicted from Eq. (14). In COMSOL we employed the frequency domain calculation available in the Wave Optics module. We first simulated the case $\Gamma_0 = 1^\circ$ and $w_D = 8$ μm over a long cell (length 200 μm), see Fig. 11. The confinement occurs as shown in Fig. 6(a), with the Stokes parameters converging in a smooth way. To save time, we then switched to shorter cells (length 60 μm along the propagation direction) to validate the FDTD simulations versus the maximum rotation angle Γ_0. To further relax the numerical requirements, we focused on the case $w_D = 8$ μm. In both the simulators, we took a Gaussian beam placed in $z = 0$ μm in air, whereas the twisted material starts at $z = 2$ μm. Figure 12 shows the intensity cross-section computed in $z = 50$ μm with FDTD (green dashed lines) and FEM (red solid lines). A very good agreement is found between the two methods. Small differences can be seen on the tails, with the FEM case showing some ripples. This is due to the perfectly matched layer (PML) boundary conditions, inducing non-negligible back reflections from the edges of the grid. Such reflections increases with Γ_0, explaining the growing differences in the tails of the predicted field. Figure 13 provides more details. The full intensity distribution in the plane xz shows some small difference in the beam amplitude, see Fig. 13(a). Beyond the numerical reflections discussed above, small discrepancies can be ascribed to slightly different definitions of the input Gaussian beam. The Stokes parameters versus z are very smooth in the case of the FDTD, whereas fast variations are observed in the FEM results, see Fig. 13(b). This validates our previous statement that in the FEM simulations the spurious numerical reflection from the grid edges are much stronger than in the FDTD, at least for the PML parameters (default setting) we chose. Indeed, the back reflections are greatly reduced when an air buffer is inserted between the PML and the twisted material (condition we used in the plotted results), demonstrating that the standard PML does not work properly in our case. Summarizing, the case of light propagating in a twisted anisotropic material is highly demanding from a numerical point of view, even in the linear regime: extreme attention should be paid when numerical simulations are performed in these geometries.

[1] A. Yariv and P. Yeh, *Optical Waves in Crystals* (Wiley, New York, 1984).

[2] R. C. Jones, A new calculus for the treatment of optical systems I. Description and discussion of the calculus, J. Opt. Soc. Am. **31**, 488 (1941).

[3] M. V. Berry, Pancharatnam, virtuoso of the Poincaré sphere: An appreciation, Curr. Sci. **67**, 220 (1994).

[4] R. Bhandari, Polarization of light and topological phases, Phys. Rep. **281**, 1 (1997).

[5] E. Cohen, H. Larocque, F. Bouchard, F. Nejadsattari, Y. Gefen, and E. Karimi, Geometric phase from Aharonov–Bohm to Pancharatnam–Berry and beyond, Nat. Rev. Phys. **1**, 437 (2019).

[6] M. Berry, Quantal phase factors accompanying adiabatic changes, Proc. Royal Soc. A **392**, 45 (1984).

[7] S. Pancharatnam, Generalized theory of interference, and its applications, Proc. Indian Acad. Sci. A **44**, 247 (1956).

[8] C. P. Jisha, S. Nolte, and A. Alberucci, Geometric phase in optics: From wavefront manipulation to waveguiding, Laser Photonics Rev. **15**, 2100003 (2021).

[9] Z. Bomzon, V. Kleiner, and E. Hasman, Pancharatnam–Berry phase in space-variant polarization-state manipulations with subwavelength gratings, Opt. Lett. **26**, 1424 (2001).

[10] L. Marrucci, C. Manzo, and D. Paparo, Optical Spin-To-Orbital Angular Momentum Conversion In Inhomogeneous Anisotropic Media, Phys. Rev. Lett. **96**, 163905 (2006).

[11] L. Marrucci, C. Manzo, and D. Paparo, Pancharatnam–Berry phase optical elements for wavefront shaping in the visible domain: Switchable helical modes generation, Appl. Phys. Lett. **88**, 221102 (2006).

[12] J. Kim, Y. Li, M. N. Miskiewicz, C. Oh, M. W. Kudenov, and M. J. Escuti, Fabrication of ideal geometric-phase holograms with arbitrary wavefronts, Optica **2**, 958 (2015).

[13] N. Yu and F. Capasso, Flat optics with designer metasurfaces, Nat. Mater. **13**, 139 (2014).

[14] A. Arbabi, Y. Horie, M. Bagheri, and A. Faraon, Dielectric metasurfaces for complete control of phase and polarization with subwavelength spatial resolution and high transmission, Nat. Nanotechnol. **10**, 937 (2015).

[15] M. Tymchenko, J. S. Gomez-Diaz, J. Lee, N. Nookala, M. A. Belkin, and A. Alù, Gradient Nonlinear Pancharatnam–Berry Metasurfaces, Phys. Rev. Lett. **115**, 207403 (2015).
[16] P. Genevet, F. Capasso, F. Aieta, M. Khorasaninejad, and R. Devlin, Recent advances in planar optics: From plasmonic to dielectric metasurfaces, Optica **4**, 139 (2017).
[17] G. F. Calvo and A. Picón, Spin-induced angular momentum switching, Opt. Lett. **32**, 838 (2007).
[18] E. Karimi, B. Piccirillo, L. Marrucci, and E. Santamato, Light propagation in a birefringent plate with topological charge, Opt. Lett. **34**, 1225 (2009).
[19] S. Slussarenko, A. Alberucci, C. P. Jisha, B. Piccirillo, E. Santamato, G. Assanto, and L. Marrucci, Guiding light via geometric phases, Nat. Photonics **10**, 571 (2016).
[20] A. Alberucci, C. P. Jisha, L. Marrucci, and G. Assanto, Electromagnetic confinement via spin-orbit interaction in anisotropic dielectrics, ACS Photonics **3**, 2249 (2016).
[21] H. Abbaszadeh, M. Fruchart, W. van Saarloos, and V. Vitelli, Liquid-crystal-based topological photonics, Proc. Natl. Acad. Sci. USA **118**, e2020525118 (2021).
[22] C. P. Jisha, A. Alberucci, J. Beeckman, and S. Nolte, Self-Trapping of Light Using the Pancharatnam–Berry Phase, Phys. Rev. X **9**, 021051 (2019).
[23] F. Simoni, *Nonlinear Optical Properties of Liquid Crystals* (World Scientific, Singapore, 1997).
[24] K. Fang, Z. Yu, and S. Fan, Realizing effective magnetic field for photons by controlling the phase of dynamic modulation, Nat. Photonics **6**, 782 (2012).
[25] M. C. Rechtsman, J. M. Zeuner, A. Tünnermann, S. Nolte, M. Segev, and A. Szameit, Strain-induced pseudomagnetic field and photonic Landau levels in dielectric structures, Nat. Photonics **7**, 153 (2013).
[26] N. Schine, A. Ryou, A. Gromov, A. Sommer, and J. Simon, Synthetic Landau levels for photons, Nature (London) **534**, 671 (2016).
[27] Q. Lin and S. Fan, Light Guiding by Effective Gauge Field for Photons, Phys. Rev. X **4**, 031031 (2014).
[28] C. V. Sukumar and D. M. Brink, Spin-flip transitions in a magnetic trap, Phys. Rev. A **56**, 2451 (1997).
[29] J. D. Hunter, Matplotlib: A 2D graphics environment, Comput. Sci. Eng. **9**, 90 (2007).
[30] J. H. Shirley, Solution of the Schrödinger equation with a Hamiltonian periodic in time, Phys. Rev. **138**, B979 (1965).
[31] A. F. Oskooi, D. Roundy, M. Ibanescu, P. Bermel, J. D. Joannopoulos, and S. G. Johnson, MEEP: A flexible free-software package for electromagnetic simulations by the FDTD method, Comput. Phys. Commun. **181**, 687 (2010).
[32] COMSOL AB, Comsol multiphysics® (2021).
[33] A. Forbes, M. de Oliveira, and M. R. Dennis, Structured light, Nat. Photonics **15**, 253 (2021).
[34] C. C. Tartan, P. S. Salter, T. D. Wilkinson, M. J. Booth, S. M. Morris, and S. J. Elston, Generation of 3-dimensional polymer structures in liquid crystalline devices using direct laser writing, RSC Adv. **7**, 507 (2017).
[35] Z. He, G. Tan, D. Chanda, and S.-T. Wu, Novel liquid crystal photonic devices enabled by two-photon polymerization, Opt. Express **27**, 11472 (2019).
[36] B. Berteloot, I. Nys, G. Poy, J. Beeckman, and K. Neyts, Ring-shaped liquid crystal structures through patterned planar photo-alignment, Soft Matter **16**, 4999 (2020).
[37] M. Sakakura, Y. Lei, L. Wang, Y.-H. Yu, and P. G. Kazansky, Ultralow-loss geometric phase and polarization shaping by ultrafast laser writing in silica glass, Light: Sci. Appl. **9**, 15 (2020).
[38] A. Forbes, Structured light from lasers, Laser Photonics Rev. **13**, 1900140 (2019).
[39] A. E. Willner, K. Pang, H. Song, K. Zou, and H. Zhou, Orbital angular momentum of light for communications, Appl. Phys. Rev. **8**, 041312 (2021).
[40] G. Milione, M. P. J. Lavery, H. Huang, Y. Ren, G. Xie, T. A. Nguyen, E. Karimi, L. Marrucci, D. A. Nolan, R. R. Alfano, and A. E. Willner, 4×20 Gbit/s mode division multiplexing over free space using vector modes and a q-plate mode (de)multiplexer, Opt. Lett. **40**, 1980 (2015).
[41] E. Nagali, F. Sciarrino, F. De Martini, L. Marrucci, B. Piccirillo, E. Karimi, and E. Santamato, Quantum Information Transfer from Spin to Orbital Angular Momentum of Photons, Phys. Rev. Lett. **103**, 013601 (2009).
[42] K. Y. Bliokh, D. Y. Frolov, and Y. A. Kravtsov, Non-Abelian evolution of electromagnetic waves in a weakly anisotropic inhomogeneous medium, Phys. Rev. A **75**, 053821 (2007).
[43] A. Alberucci, A. Piccardi, U. Bortolozzo, S. Residori, and G. Assanto, Nematicon all-optical control in liquid crystal light valves, Opt. Lett. **35**, 390 (2010).
[44] K. Fang and S. Fan, Controlling The Flow of Light Using the Inhomogeneous Effective Gauge Field that Emerges from Dynamic Modulation, Phys. Rev. Lett. **111**, 203901 (2013).
[45] F. Liu and J. Li, Gauge Field Optics with Anisotropic Media, Phys. Rev. Lett. **114**, 103902 (2015).
[46] Y. Chen, R.-Y. Zhang, Z. Xiong, Z. H. Hang, J. Li, J. Q. Shen, and C. T. Chan, Non-Abelian gauge field optics, Nat. Commun. **10**, 3125 (2019).
[47] Y. Lumer, M. A. Bandres, M. Heinrich, L. J. Maczewsky, H. Herzig-Sheinfux, A. Szameit, and M. Segev, Light guiding by artificial gauge fields, Nat. Photonics **13**, 339 (2019).
[48] V. Brosco, L. Pilozzi, and C. Conti, Two-flux tunable Aharonov–Bohm effect in a photonic lattice, Phys. Rev. B **104**, 024306 (2021).
[49] Z.-T. Huang, K.-B. Hong, R.-K. Lee, L. Pilozzi, C. Conti, J.-S. Wu, and T.-C. Lu, Pattern-tunable synthetic gauge fields in topological photonic graphene, Nanophotonics **11**, 1297 (2022).